Deepwell Monitoring of Strain-Sensitive Parameters over the Greater Southern California Uplift

Thomas L. Henyey, Ta-liang Teng, Douglas E. Hammond, Charles G. Sammis,
John K. McRaney, Peter E. Malin, Liang-Fang Sun,
Derek V. Manov, Laurence G. Miller, and
Nancy L. Scott

Department of Geological Sciences
University of Southern California
Los Angeles, CA 90007

USGS CONTRACT NO. 14-08-0001-16745
Supported by the EARTHQUAKE HAZARDS REDUCTION PROGRAM

OPEN-FILE NO. 81-90

U.S. Geological Survey
OPEN FILE REPORT

U.S.C. Geophysics Laboratory Tecnical
Report #80-1

Final Technical Report for U.S.G.S. Contract
#14-08-0001-16745

Deepwell Monitoring of Strain-Sensitive Parameters over the Greater Southern California Uplift

Thomas L. Henyey
Ta-liang Teng
Douglas E. Hammond
Charles G. Sammis
John K. McRaney
Peter E. Malin
Liang-Fang Sun
Derek V. Manov
Laurence G. Miller
Nancy L. Scott

Department of Geological Sciences
Uniersity of Southern California
Los Angeles, CA 90007

January, 1980

FINAL TECHNICAL REPORT

submitted to the

U. S. GEOLOGICAL SURVEY

by the

UNIVERSITY OF SOUTHERN CALIFORNIA
Department of Geological Sciences
University Park
Los Angeles, CA 90007

Contract No.:	#14-08-0001-16745
Principal Investigators:	Thomas L. Henyey Associate Professor of Geophysics
	Ta-liang Teng Professor of Geophysics
	Douglas E. Hammond Assistant Professor of Geophysics
	Charles G. Sammis Associate Professor of Geophysics
Government Technical Officer:	Jack F. Evernden
Title of Work:	DEEPWELL MONITORING OF STRAIN-SENSITIVE PARAMETERS OVER THE SOUTHERN CALIFORNIA UPLIFT
Effective Date of Contract	November 8, 1977
Contract Expiration Date:	January 7, 1980
Amount of Contract:	$392,384.00
Date:	December, 1979

TABLE OF CONTENTS

SHORT TECHNICAL DISCUSSION

The availability of abandoned and newly drilled wells within the southern California Uplift is an important resource which has been exploited by the University of Southern California. A group of particularly desirable wells has been refurbished and prepared for downhole instrumentation, for the detection of acoustic emissions, electrical and RF emissions, water level and turbidity, and subsurface temperature. We are cooperating with the USGS (Zoback) to instrument a 4000 foot well to be drilled along the San Andreas fault near Palmdale. All instruments have undergone final assembly and have been evaluated in terms of performance criteria. We are presently awaiting delivery of specially fabricated cable assemblies for continuous deployment of downhole packages. Ten holes ranging in depth from 600 - 6000 feet in a variety of geological environments from the backbone of our subsurface monitoring program. We regard this program as a preliminary step in the instrumentation of deep drill holes along the San Andreas fault and in other seismically active areas.

We regard our work to be especially pertinent to an analysis of strain in the Palmdale uplift and the search for precursors to earthquakes in southern California. The deep wells are centrally located with respect to the recently reported strain anomalies near Palmdale (eg. Savage, ARIES, etc.). Finally, the program is an important complement to our Dalton Tunnel Geophysical Observatory and proposed studies of regional tilt in the western Mojave region.

This technical report summarizes the work on this project performed under USGS Contract #14-08-0001-16745. The work is continuing on USGS Contract #14-08-0001-18383.

RESEARCH PROGRESS

A. Deep Wells

During the first two years of its deep hole recovery program, the 23 holes (Fig. 1) listed in Table 1 have been secured by U.S.C. for use in deepwell research. Previous U.S.C. Technical Reports described the methods used in securing and preparing these sites, and the geological parameters of each site. Working depths as of 2/1/80 are given in column 4 of Table 1. Figure 1 shows the distribution of wells along both sides of the San Andreas fault, and their relationship to the Palmdale uplift. As all of these holes cannot be utilized by U.S.C. on a full-time basis; selected holes are being made available to other scientists for downhole experiments. Table 2 shows the research efforts underway at each site.

B. Program Results

Our program consists of the following major research efforts:

(1) Groundwater radon-chemistry measurements

(2) Acoustic emissions detection

(3) Piezoelectric studies

(4) Comparative magnetometer studies

(5) Water level-turbidity-temperature measurements

(6) Well permeability

Much of the specific instrumentation and design of these projects have been discussed in our earlier progress reports. The following sections report on the current status of research efforts.

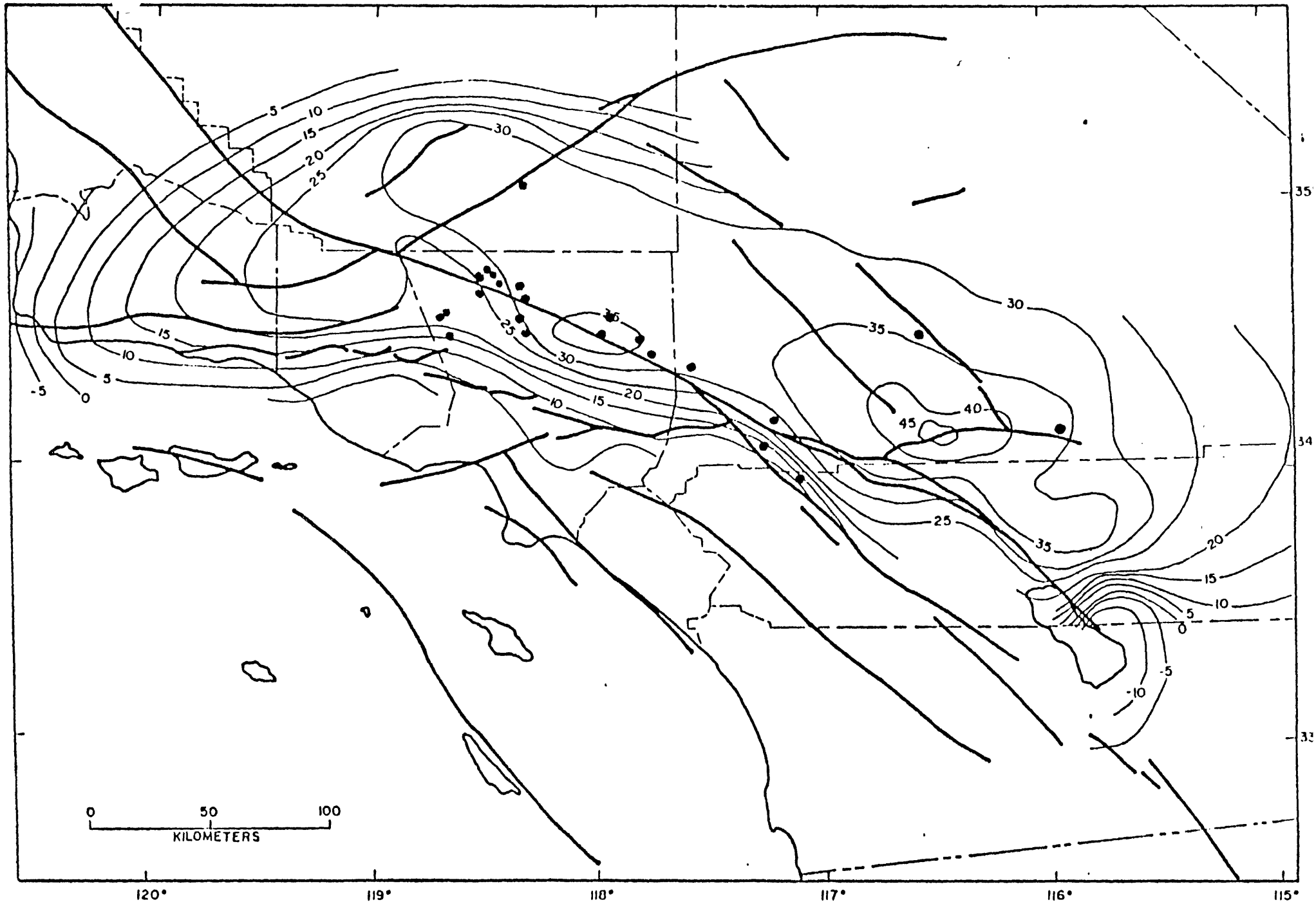
5
10
15
20
25
30
-5
0
35
40
45
0
50
100
KILOMETERS
120°
119°
118°
117°
116°
115°
35
34
33

FIGURE 1

TABLE 1

U.S.C. Deep-well Research Sites

Name	Latitude	Longitude	Depth	Lithology
Skelton	34°42'N	118°31'W	3150'	Granite
Del Sur	34°39'N	118°14'W	2300'	Sediments
Virginia Lee	34°30'N	117°49'W	1100'	Sediments
Chief Paduke	34°30'N	117°59'W	1200'	Fault Gouge
Pratty	34°31'N	118°17'W	900'	Granite
Ritter #1	34°36'N	118°15'W	150'	Fault Gouge
Ritter #2	34°36'N	118°15'W	350'	Fault Gouge
Handley	34°25'N	117°35'W	5500'	Sediments, granite
Haskell	33°57'N	117°03'W	3180'	Sediments
Brady	34°10'N	115°56'W	1350'	Sediments
Fairmont	34°46'N	118°27'W	650'	Sediments
Roy Christenson (Palmdale #1)	34°32'N	118°02'W	1100'	Sediments
Wright-Kovaleski	34°31'N	118°21'W	0'	Granite
Paradise #1	34°34'N	118°41'W	1150'	Sediments
Paradise #2	34°34'N	118°41'W	875'	Sediments
SB-2	34°15'N	117°19'W	1510'	Granite
LH-1	34°44'N	118°23'W	710'	Granite
LH-2	34°41'N	118°26'W	1200'	Granite
LH-3	34°39'N	118°29'W	1200'	Granite
LV-1	34°37'N	116°43'W	2300'	Granite
Roberts	34°38'N	118°20'W	600'	Fault Gouge
Zoback	34°28'N	117°51'W	4000'*	Granite
Shandon Hills	34°10'N	117°20'W	700'	Schist

*Not yet drilled

TABLE 2

Deep-Well Site and Instrument Deployment

Site	Air-Gun Stacking	Acoustic Emissions	Water-Level[1] Temperature Turbidimeter	Electrical Emissions	Seismometer Package	Radon Water Chemistry
Skelton	X	X	X	X	X	X
Del Sur	X	X	X		X	
Virginia Lee		X	X		X	X
Chief Paduke	X		X			X
Pratty	X					X
Ritter #1			X			X
Ritter #2	X				X	
Handley		X	X	X	X	X
Haskell		X	X		X	X
Brady		X	X			
Fairmont		X			X	X
Roy Christenson						X
Wright-Kovaleski		X	X		X	
Paradise #1						X
Paradise #2						X
SB-2			X[1]			
LH-1			X[1]			
AN-1				X		
Roberts		X		X		
Zoback	X	X		X		
Shandon		X		X		

[1]Only temperatures to be measured in these cased holes.

GROUNDWATER CHEMISTRY

The following have been accomplished during the previous year:

1) Monitoring of radon and groundwater chemistry has been initiated in two deep wells, Fairmont and Virginia Lee.

2) The concentration of ionic constituents in samples from the U.S.C. radon network versus time has been extended for the Seminole Springs, Arrowhead Springs, and Big Pines sites.

3) Analyses to date have been synthesized. The synthesis forms the next portion of this section.

Recent studies by Russian, Chinese, and Icelandic groups (reviewed by Teng, 1980) have suggested that the radon concentration in groundwater may increase prior to earthquakes, and thus radon may serve as a precursory signal for seismic events. The mechanism (or mechanisms) responsible for such increases has not yet been elucidated, but several factors which may play a role have been discussed by Tanner (1979). They include: (1) an increase in the surface area/pore volume of rocks near the source area, resulting in increased radon emanation per unit volume of pore fluid, (2) the response of groundwater flow patterns and flow rates to either fracturing of strain accumulation, and (3) the response to environmental phenomena such as rainfall, temperature, and atmospheric pressure fluctuations. As such we have monitored certain chemical constituents together with radon concentration in one well and three springs (Table 3) in southern California. Water chemistry should be sensitive to flow patterns as waters from different horizons mix.

TABLE 3

ARP Well (AR) - near Sierra Madre fault in sandy soil underlain by crystalline rock. Samples taken from a wellhead pumped by the Metropolitan Water District.

Arrowhead Springs (AS) - in the San Bernardino Mountains near San Andreas fault in crystalline rock. Samples taken from a pipe which taps a hot spring ($T = 74^{\circ}c$).

Big Pines (BP) - in the San Bernardino Mountains, within 1 km of the San Andreas fault zone, in sandy soil underlain by crystalline rock. Samples are drawn from well-head of a pump which periodically supplies water for the Big Pines campground.

Seminole Hot Springs (SH) - in the Santa Monica Mountains in sandy soil underlain by sedimentary rocks. Samples ($T \simeq 40^{\circ}c$) are drawn from the outlet jet of a pump which supplies water to a pool.

Ten sites have been monitored for radon over periods from one to three years (Figure 2). These sites were selected for their proximity to major faults, coverage of a wide geographic area, and suitability of sampling. Duplicate radon samples are collected by volunteers in the field and either mailed or hand carried to U.S.C. Sample bottles are one liter aluminum bottles fitted with inlet and outlet tubes. Bottles are filled either by evacuating the container and drawing water with the vacuum or by slowly filling an unevacuated bottle through a tube inserted to the bottom of the bottle. Radon is measured in the laboratory using standard techniques described elsewhere. The water remaining after radon extraction is stored in acid-cleaned glass bottles for later analysis of cations and anions.

Four of the radon sites were selected for time-dependent cation (Na^+,K^+,Ca^+) and anion (Cl^-) analysis, on the basis of the behavior of radon and the location of the sample site. Calcium showed considerable variability with time, probably due to $CaCO_3$ precipitation during radon analyses, and these data are of little value. Potassium variations were essentially the same as those observed for sodium.

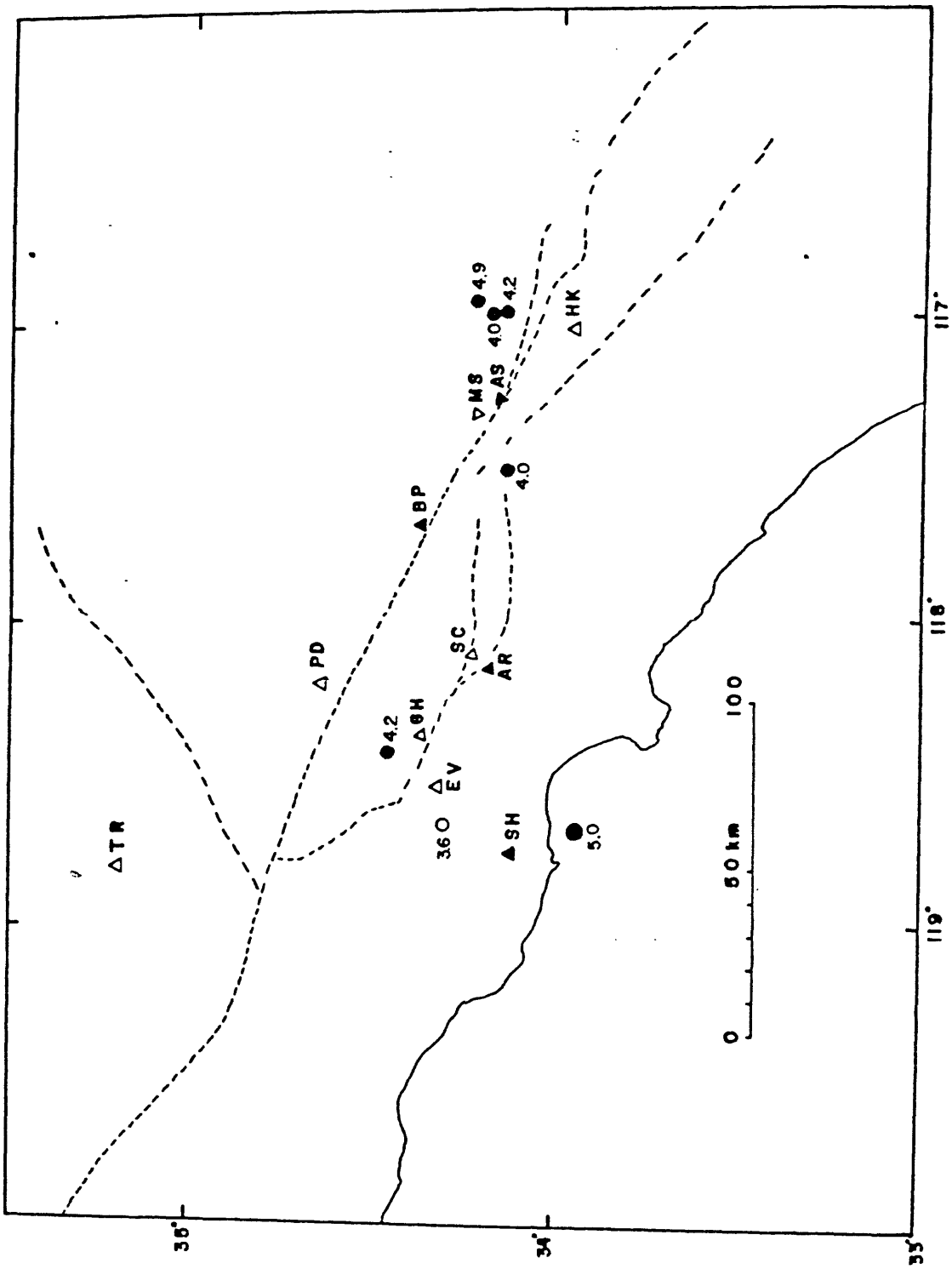

FIGURE 2. Index map of southern California wells and springs with long-term radon records are located by triangles and identified by code letters. Stations discussed in detail are solid triangles. The epicenters of significant earthquakes occurring within the monitoring period are also shown. Dashed lines trace the San Andreas fault zone (SA), San Jacinto fault (SJ), Garlock fault (GA) and San Gabriel fault (SG).

FIGURE 2

Data from the four sampling sites are shown in figures 3-6, along with pertinent environmental variables. Seismic events are indicated by arrows. The likelihood of strain accumulation influencing a particular site will depend on geological and hydrological factors. The probability of observing a radon anomaly prior to an earthquake might be proportional to the strain energy released and inversely proportional to the area over which strain energy is accumulated. Directional factors are probably important also. As a qualitative index of the probability of observing a seismically induced radon anomaly, the following probability function was used:

$$P = \frac{\exp (3.4\ M)}{1000\ R^2}$$

where M - earthquake magnitude (Richter scale)

R - separation of monitoring site and epicenter (km)

Numerical values of this function were calculated for all earthquakes ($M > 3.5$) in the study area. The largest value observed was at Seminole Hot Springs where $P = 60$ for the Malibu earthquake (1-1-79 $M = 5.0$). At the sites studied in detail only two values of $P > 10$ were observed and six values of $P > 1$ were observed. These are indicated by arrows in figures 3-6. Epicentral locations are indicated in figure 2.

Results of concentrations vs. time at the ARP well are shown in figure 3. Radon at this site shows a close relationship to rainfall. When it rains, radon concentrations are low and when it is dry, radon concentrations are high. This suggests that groundwater is diluted by fresh rainfall, but analysis of ionic constituents over one of these cycles shows no evidence of dilution. An alternative explanation is that the concentrations of ionic species are controlled by processes in a soil zone. Radon concentrations primarily reflect the history of aquifer waters for the week prior to sample

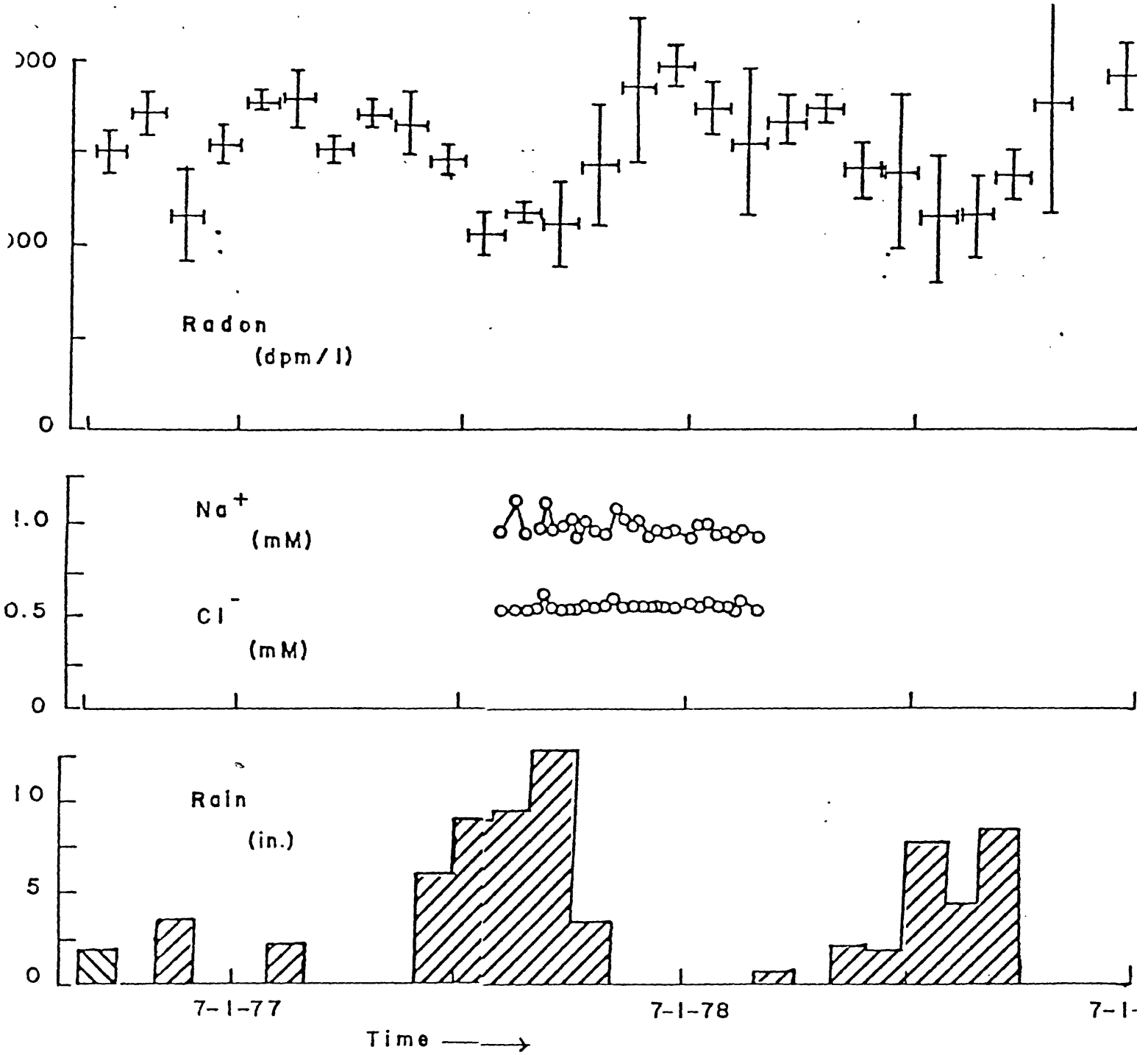

FIGURE 3. Radon sodium chloride, and rainfall vs. time at the ARP well (AR). Radon concentrations show the monthly averages (±1σ) of 3-5 samples. Rainfall is the monthly total at a station in Pasadena.

FIGURE 3

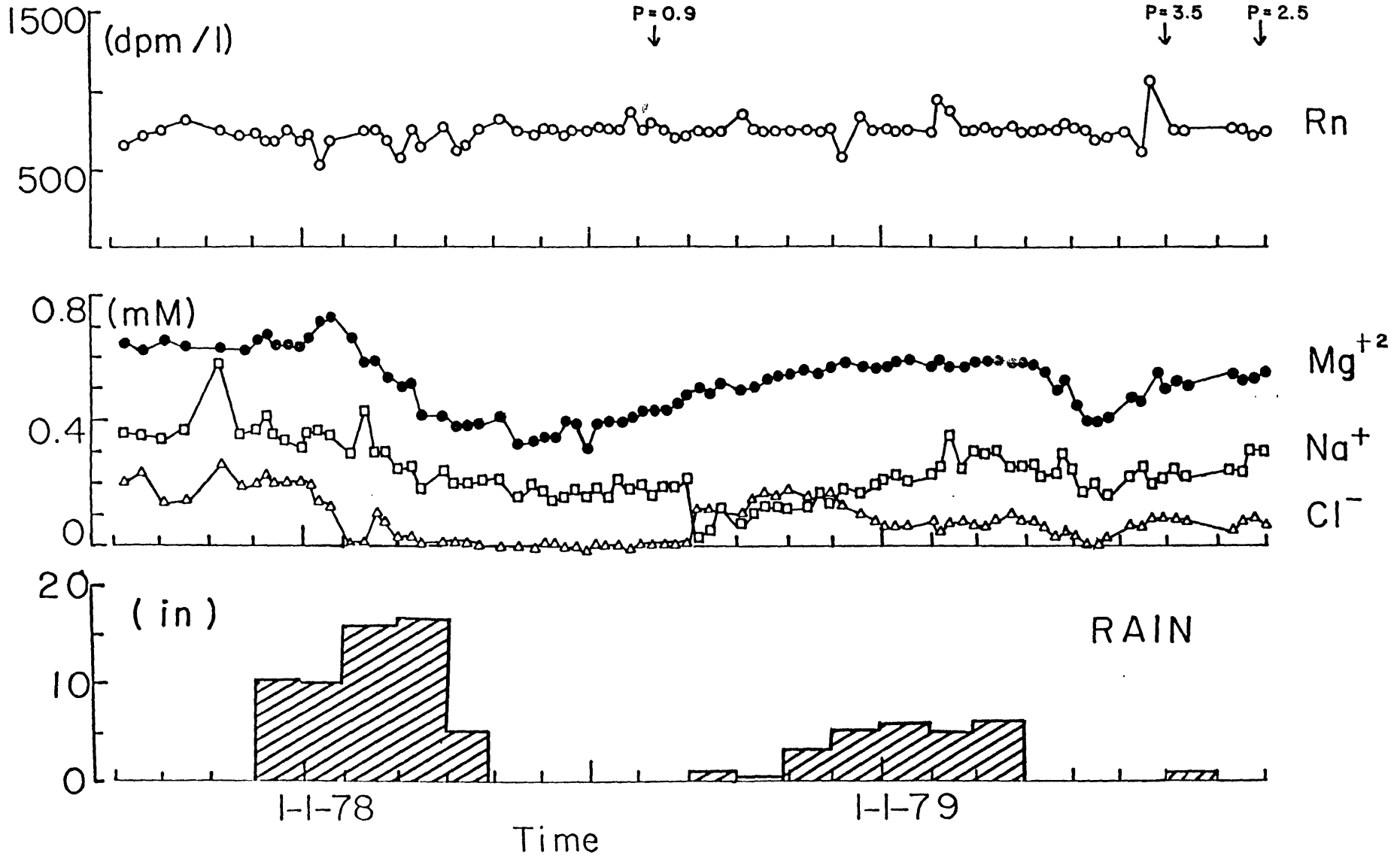

FIGURE 4. Radon, magnesium, sodium, chloride and rainfall vs. time at Big Pines (BP). Rainfall is the monthly total at the Big Pines Forest Service Station. P is discussed in the text.

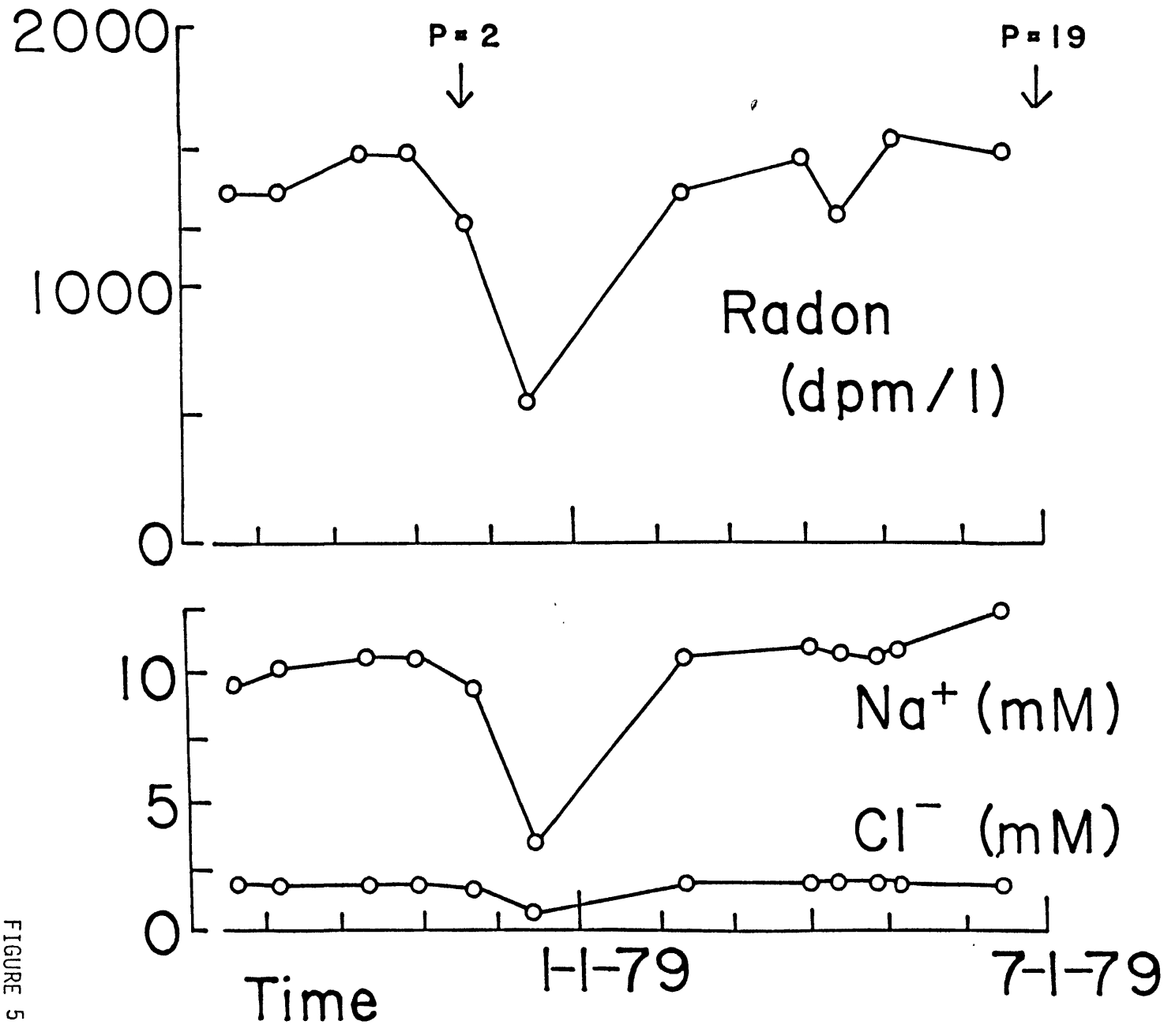

FIGURE 5. Radon, sodium, and chloride vs. time at Arrowhead Springs (AS).

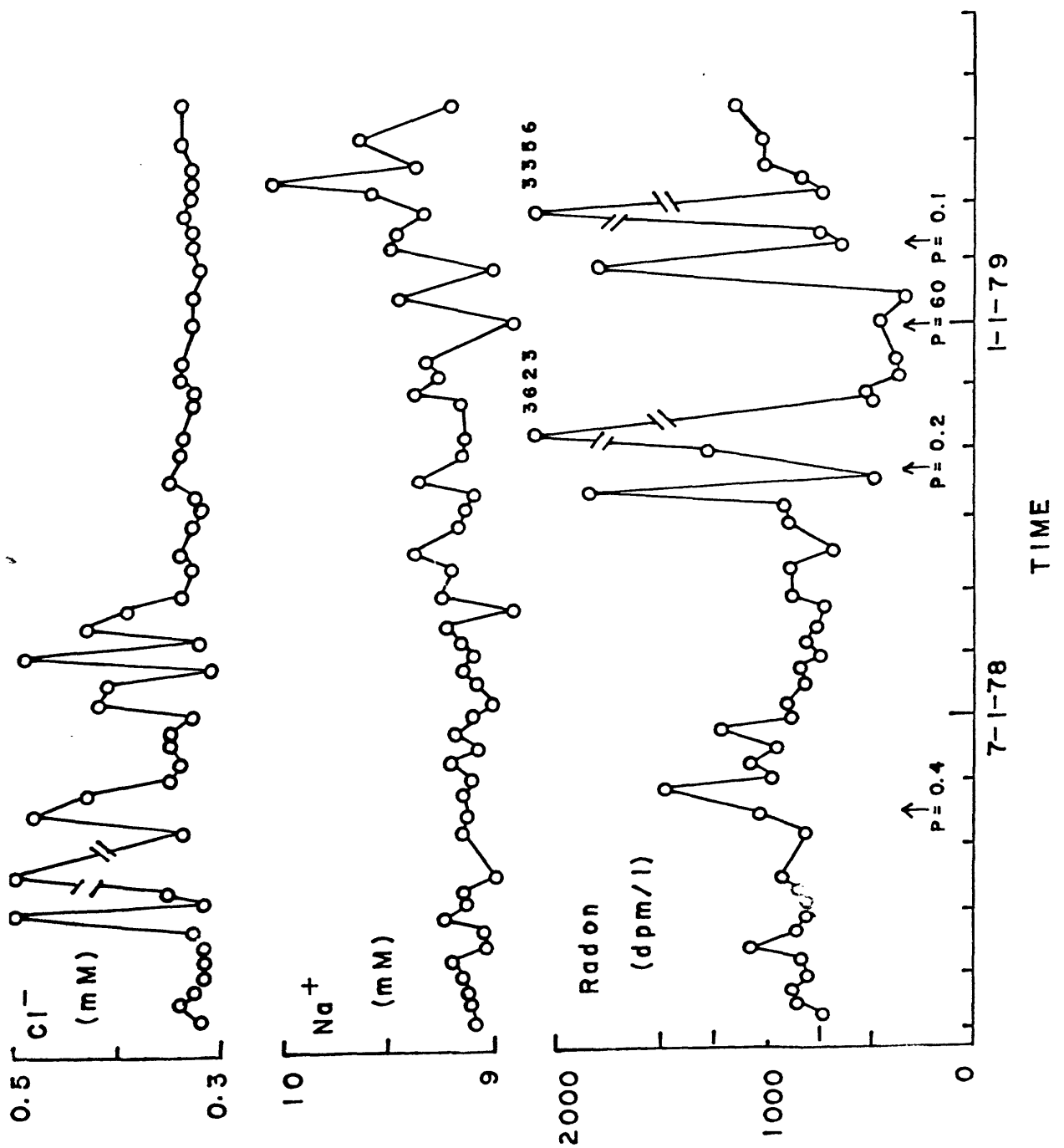

FIGURE 6. Radon, sodium and chloride vs. time at Seminole Hot Springs (SH). P is discussed in the text.

FIGURE 6

collection. If the equilibrium concentration of radon is low in a zone where ionic constituents are acquired and the residence time is long, and if the equilibrium radon concentration is high in an aquifer zone where the residence time is short and variable, the observed data for this site are easily explained. High rainfall results in a short aquifer residence time and low radon concentrations. This data suggests that radon can vary in response to groundwater flow rates.

The Big Pines site (figure 4) also shows a response to rainfall. At this site, however, concentrations of ionic constituents decrease in response to rainfall, but radon shows no change. All ionic constituents decrease several months after the onset of winter rains, and then increase during dry months. All elements show phase lags relative to rainfall. Chloride responds most quickly and shows the largest fractional changes, while magnesium and sodium show longer phase lags and smaller fractional variations. The phase lag in time is smaller in 1978 when rainfall was greater than in 1979. These observations suggest that at this site, the residence time of water in the soil zone, where ionic constituents are acquired, is short (several months) and variable. Cation concentrations are buffered by ion exchange processes and chloride is not well buffered. However, the residence time of water in the flowing aquifer is sufficiently long during all seasons that no change in radon is observed. This site was 70 km from the Big Bear earthquake (6-30-79, M = 4.9, P = 3.5). A small radon anomaly was observed in the sample collected 8 days prior to the event. Another sample was collected one day prior to this event, but was delayed for 6 weeks in the mail. This data (not plotted) also suggested high radon concentrations, but the low levels of radon remaining when the sample was received and the uncertainties in blanks preclude definite conclusions about the radon behavior prior to the event.

Data from the Arrowhead Springs site (figure 5) shows one large fluctuation in December, 1978. This sample shows concentrations of radon and ionic constituents which are only 40% of normal. Apparently this sample was diluted, but how this dilution occurred is not clear. This site was closer to the Big Bear earthquake (30 km), but no unusual radon behavior was observed. It should be noted, however, that the sampling interval is 3-4 weeks at this site and short-lived spikes in radon concentrations could be missed.

Data from the Seminole Hot Springs site is plotted in figure 6. Eleven months of radon data prior to the period plotted showed fairly uniform concentrations, are ($\pm 1\sigma$) = 1008±237. Large fluctuations were observed after October, 1978. Values ranging from 0.5 to 4 times the average were observed prior to and following the Malibu earthquake (1-1-79, M = 5.0, P = 60). Ionic constitutents showed no fluctuations (note expanded scales) during this period. The high chloride values in early 1978 are probably due to sulfide interference. This problem was eliminated in later analyses. The cause of the radon fluctuations is not obvious, although it could be related to strain accumulation. It is possible that different sources of water were reaching the surface, although the constancy of ionic constitutents makes this appear to be an unlikely explanation. Fluctuations could be caused by variations in the transit time to the surface from zones adding large amounts of radon to these thermal waters. Fluctuations could also be caused by collecting samples containing variable amounts of gas. Duplicate samples showing the large increases only agreed within 25%, which is far above the normal precision. Poreda et al. (1978) have demonstrated the presence of additional gases associated with high radon concentration in thermal springs. However, this mechanism is less likely to produce the low concentrations of radon observed, unless samples collected prior to October 1978 had a very constant fraction of gas phase collected with the

water sample (about 15% by volume) and samples collected from mid-November, 1978 to mid-January, 1979 had almost no gas phase collected. Fluctuations could also be caused by microfracturing of rocks, producing fluctuations in the rate of radon emanation from rocks. At present it is not possible to distinguish which, if any, of these mechanisms caused the radon fluctuations.

The following conclusions may be inferred from our data.

1) Radon concentrations in cold springs can respond to precipitation, apparently due to changes in aquifer flow rates. Ionic constituents need not show any response.

2) Ionic constituents of groundwater may show changes in response to precipitation, apparently due to changes in the residence time of water in the soil zone. These changes need not be accompanied by changes in radon concentrations.

3) Anomalous radon behavior was observed in a thermal spring prior to and following the Malibu earthquake. No variation in the concentrations of ionic constituents was observed, suggesting that the mechanism causing this event is probably not mixing of different groundwaters. Analysis of seismic activity in proximity to sampling sites indicates that this site is the one most likely to show anomalous behavior.

ACOUSTIC EMISSIONS - NANOEARTHQUAKES

The high frequency, wide band (20 Hz-15 kHz) recording instruments for the detection of acoustic emissions which we have developed were deployed in three deep wells located within seismically active regions. Two sites are close to the San Andreas fault - the 400 meter Skelton well (uncased in granite, recently deepened to 1 km) and the 700-meter Del Sur well (cased in sediment) near Palmdale, California. The third site, a 1.1 km deep uncased well in granite near Monticello, South Carolina is of particular interest due to its proximity to a large reservoir believed to be triggering seismicity from reservoir impounding. The bottom of the Monticello well is thought to be within 1 km to the hypocenter cluster.

Our acoustic emission recorder is designed to observe and study the nature of underground acoustic signals within the frequency band 20 Hz to 15 kHz. The detailed circuit diagrams were given in an earlier U.S.C. Geophysical Laboratory Technical Report No. 77-7. Due to the high frequency band of interest, it is impractical to use telephone telemetry for laboratory recording and an in situ recording mode has been adopted. A simplified block diagram of the system is shown in Figure 6a. The acoustic signals are picked up by a broad-band (1 Hz to 100 kHz) hydrophone placed at the bottom of the well. One stage of preamplifier with 40 db gain is applied to the signal right next to the sensor so as to avoid spurious signals entering into the system through the long downhole signal cable connecting the sensor to the surface recording system. The recording system normally operates in a standby mode. When signal amplitude exceeds a pre-set level, the event detector triggers and sends a pulse to start an instrumental-quality tape recorder. A digital delay is employed to momentarily halt the data traffic by 500 ms. The tape recorder has two tracks, one for the delayed acoustic signal and the other for the time code generated by a calendar clock. The entire recording system is packaged in a 26" x 20" x 16" fiberglass case for field use. Four of these acoustic recording

systems have been constructed and placed through numerous laboratory and field tests.

In all three wells, numerous acoustic emissions were detected with dominant spectral energy in the band 0.5 to 5 kHz and a peak about 2 kHz. These events have durations on the order of milliseconds and waveforms similar to a local earthquake greatly scaled down in size. Their spectra and waveforms for different events are very similar, except for events from the cased Del Sur well. The events from the Del Sur well are more pulse-like; they may have been generated by a mechanism different from the generation of acoustic emissions through microcracking. A mechanism of casing-wall rock interaction may be involved. Signals from the other two wells are much more interesting and resemble greatly scaled-down seismic events. During the recording period, at least 30 events per day were recorded in the Skelton well and 500 events per day in the Monticello well. Due to the single station recordings, we are not yet able to ascertain how far the acoustic emission sources are from the well-bottom sensor. Efforts will be made in the future to obtain more information on the source distance using two or more acoustic sensors.

Illustrated data were obtained from the Skelton well (May 2-4, 1979) the Monticello well (May 11-13, 1979), and the Del Sur well (August 2-17, 1978). Data from the Del Sur well recorded the M 5.3 Santa Barbara event (August 13, 1978) and its aftershocks plus numerous induced disturbances. Samples of the recordings during the Santa Barbara event have been presented in an earlier U.S.C. Semi-Annual Technical Report November, 1978, USGS Contract No. 14-08-0001-16745.

Examples of the time traces and respective spectra are shown in figures A1 to A6 for the Skelton, California events, figures A7 to A12 for the Monticello, South Carolina events. A 1 kHz low cut filter has been applied to remove spurious noise. The duration of the waveforms is normally 5 to 10 ms and their amplitude is typically on the order of 10 μ bar. The larger events may be 5 to 10 times longer in duration; however, amplitudes are clipped which make it difficult to estimate the actual size of these clipped events. It is seen that the dominant energy peak occurs around 2 kHz and drops off sharply in the low-frequency end due mostly to the low-cut filter. Toward the high-frequency end, the spectrum drops off exponentially with an occasional secondary peak. Little energy exists beyond 6 kHz. Only very rarely are there pulse-like events recorded resulting in a broad spectrum.

One interesting finding is that these acoustic signals have very similar waveforms and spectra whether they are from the Skelton well of California or from the Monticello well of South Carolina. These waveforms resemble greatly scaled-down seismic events. Assuming the validity of downward extrapolation of duration time vs. magnitude relationships, these events would have magnitudes in the range -3 to -5; and as such, we call them nanoearthquakes. Work is also presently in progress to determine the temporal relationships between individual events, and their relationships to any nearby microearthquakes - particularly for the Monticello well.

Continuous deployment of four completed acoustic emission recording units and four additional under construction is awaiting delivery of some cable with specially constructured terminations.

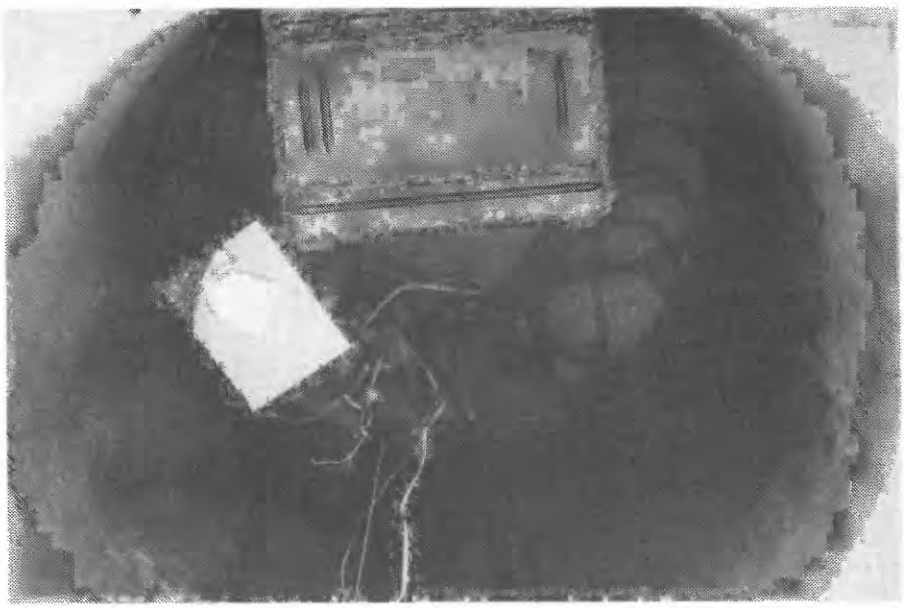

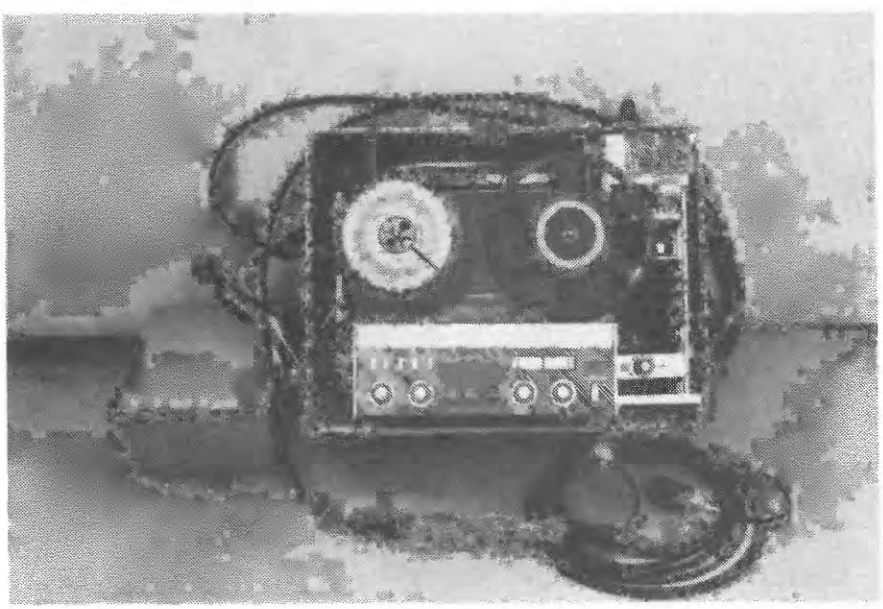

Acoustic Emission Records

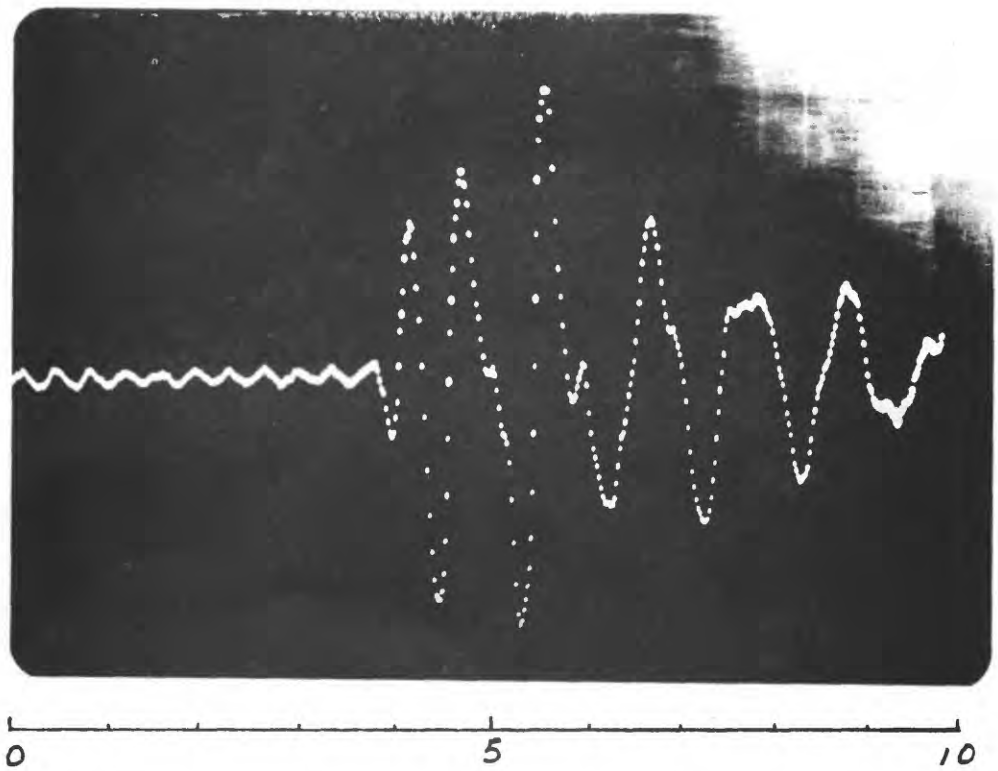

Time Function

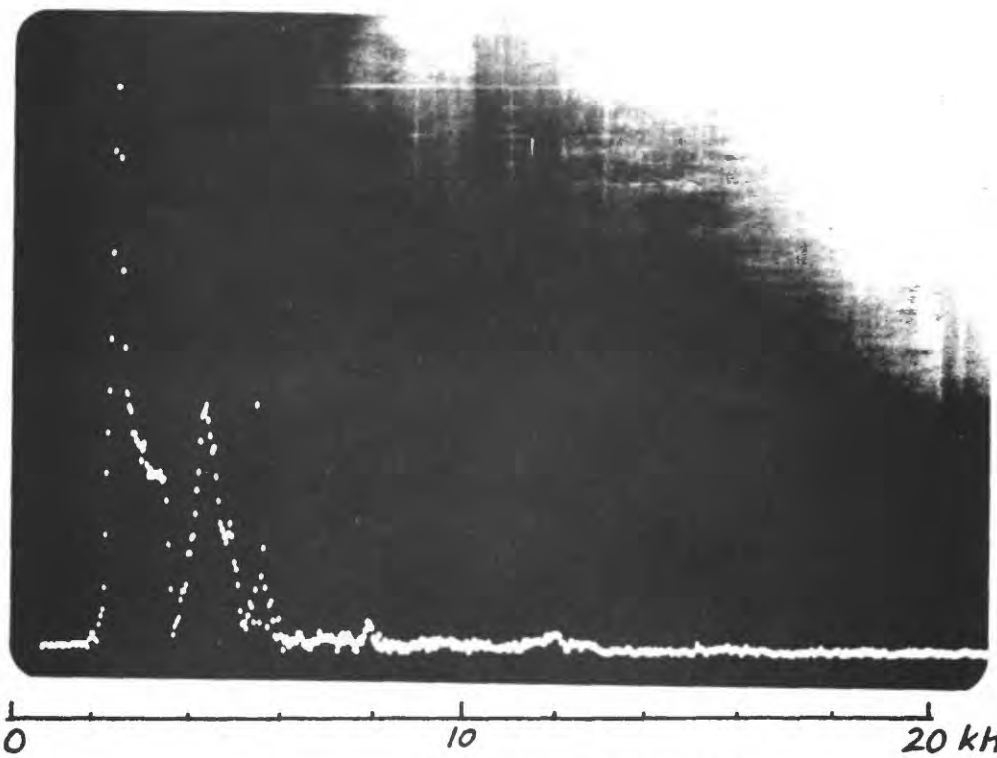

Spectrum

Fig. A1

Acoustic Emission Records

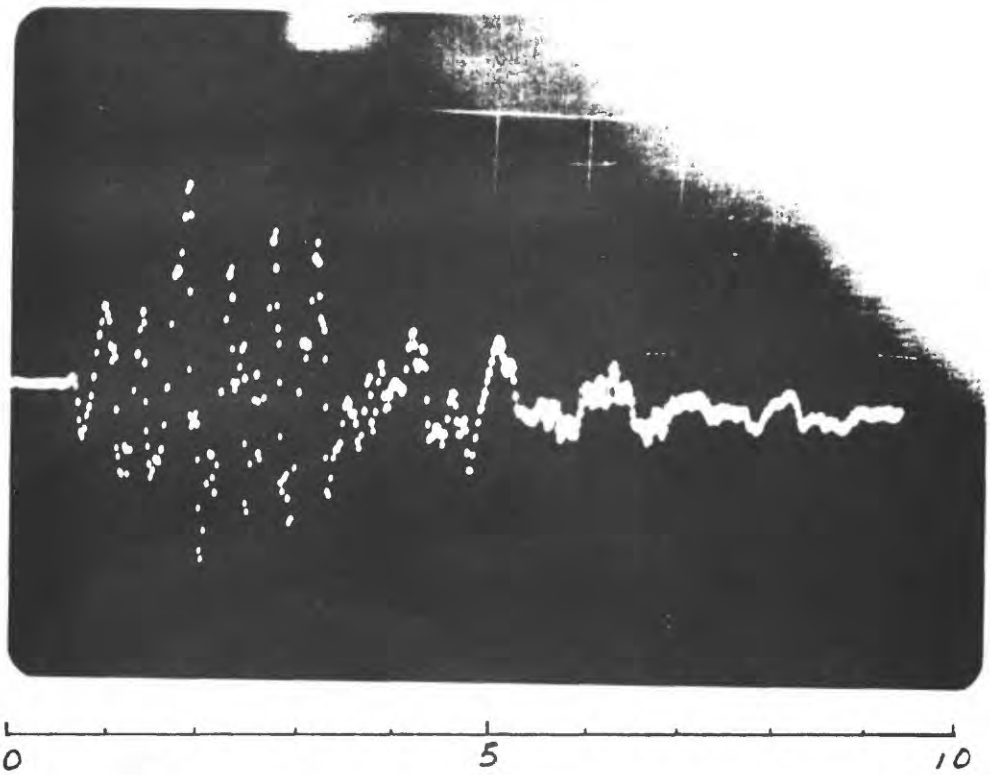

Time Function

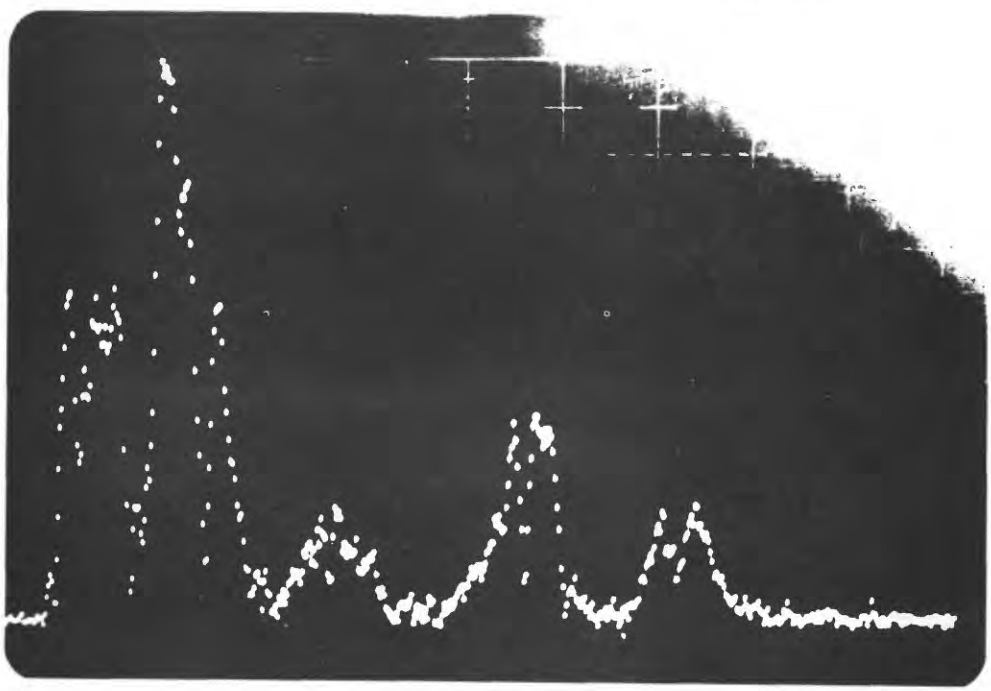

Spectrum

Fig. A2

Acoustic Emission Records

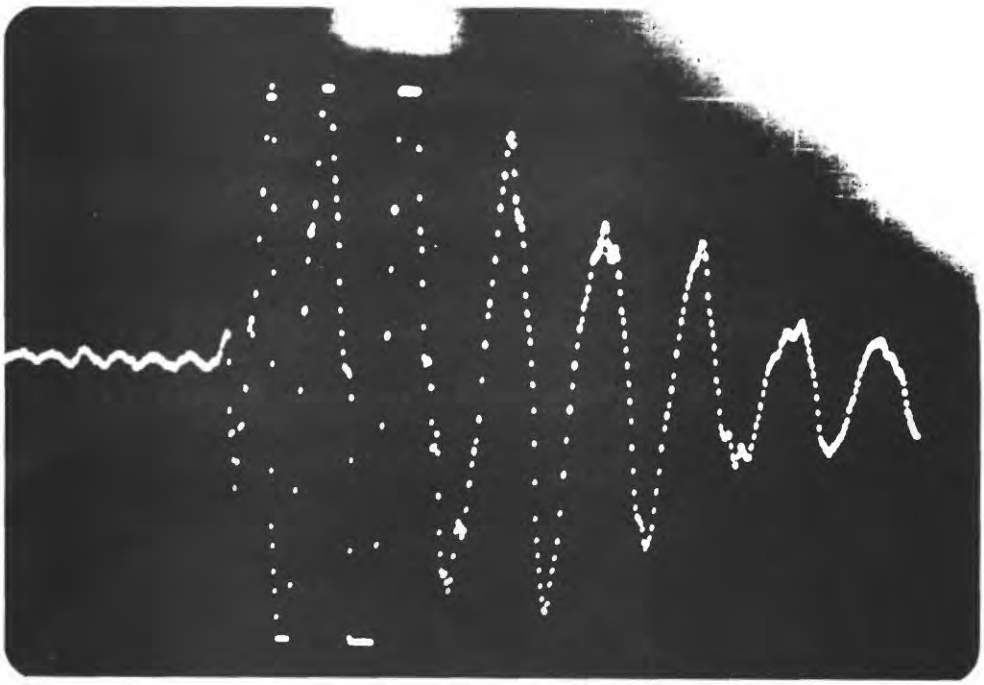

Time Function

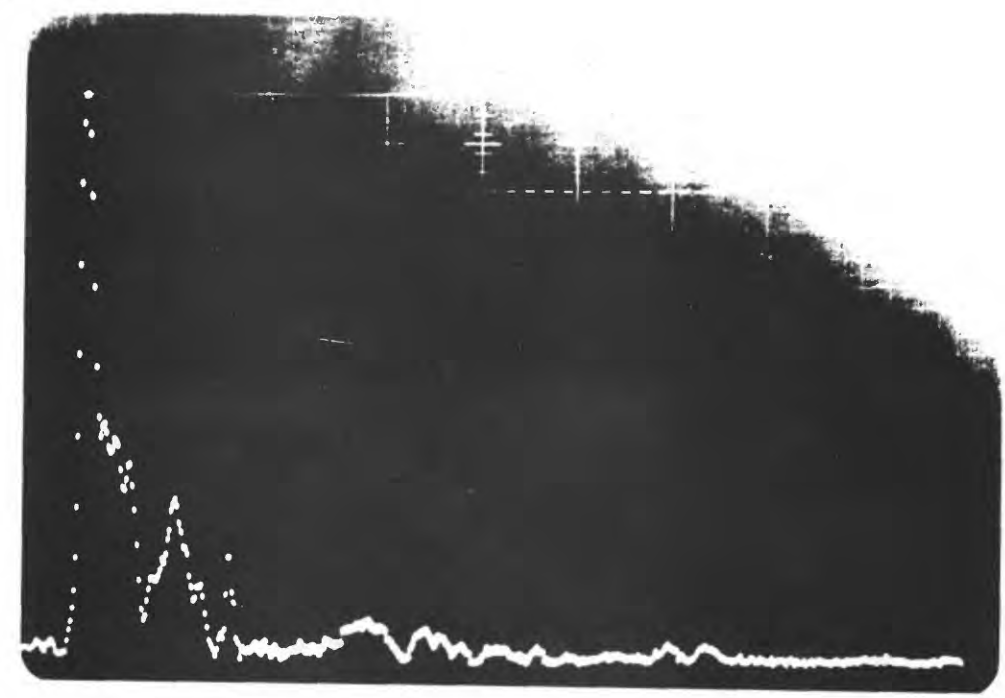

Spectrum

Fig. A3

Acoustic Emission Records

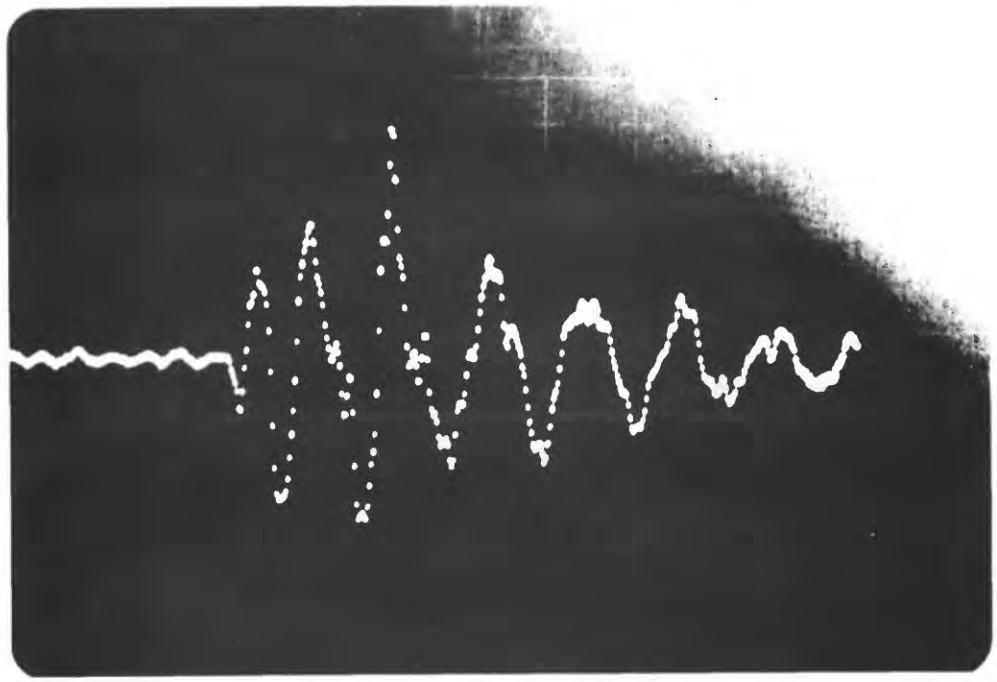

Time Function

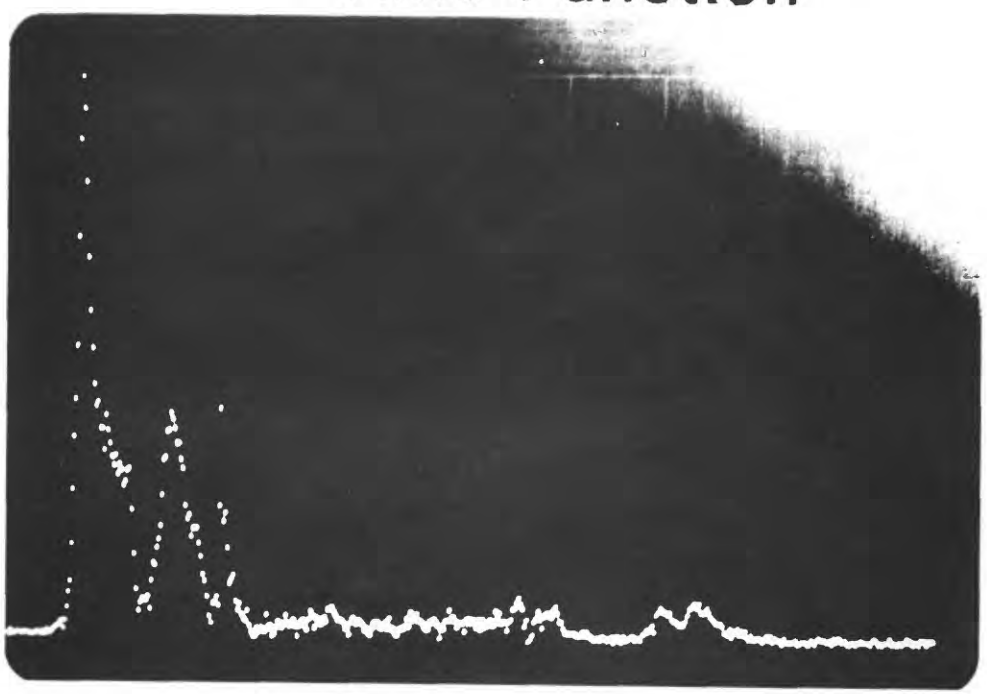

Spectrum

Fig. A4

Acoustic Emission Records

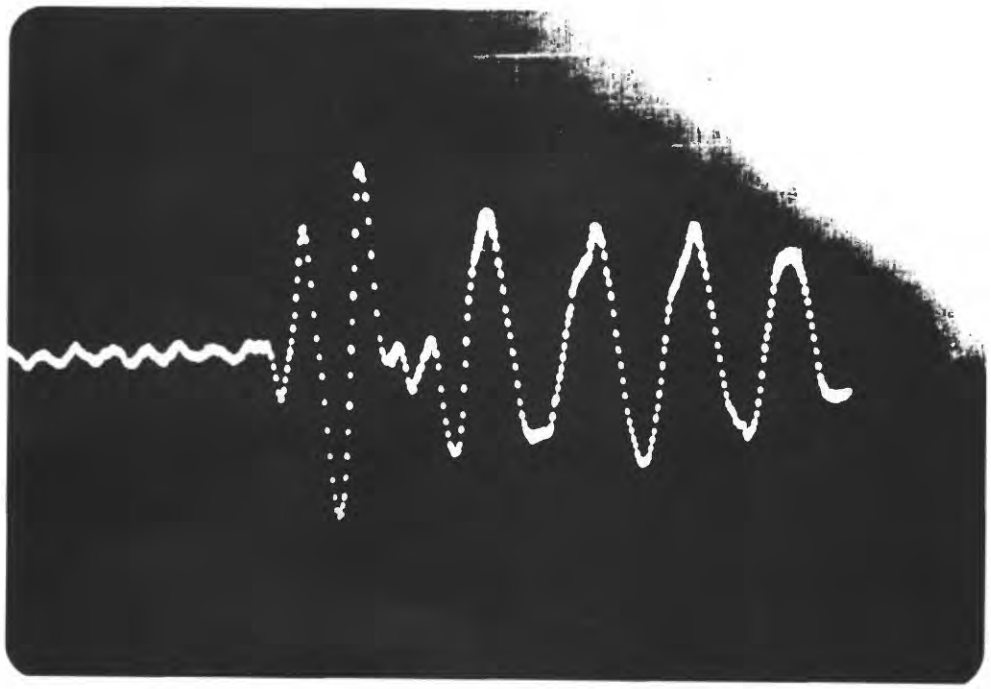

Time Function

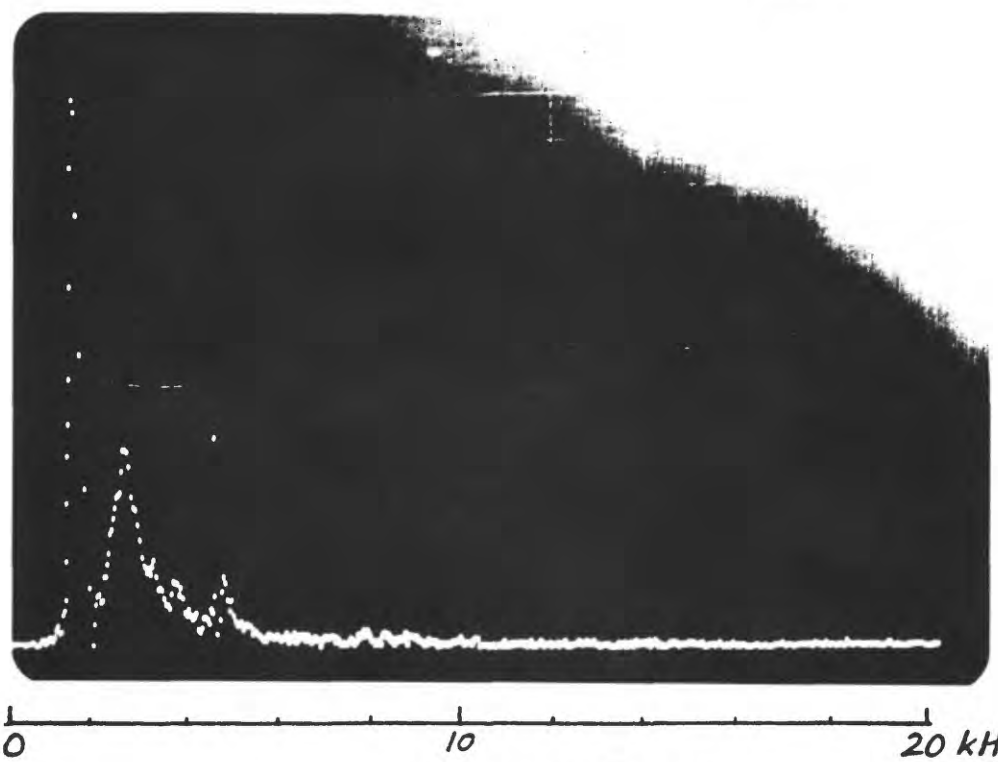

Spectrum

Fig. A5

Acoustic Emission Records

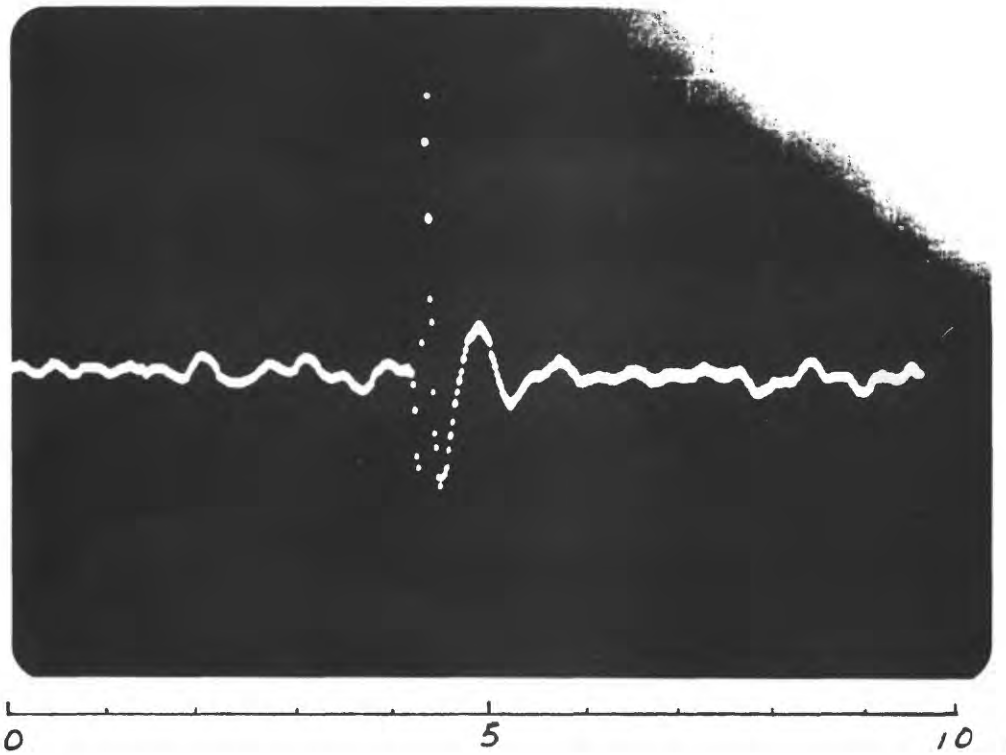

Time Function

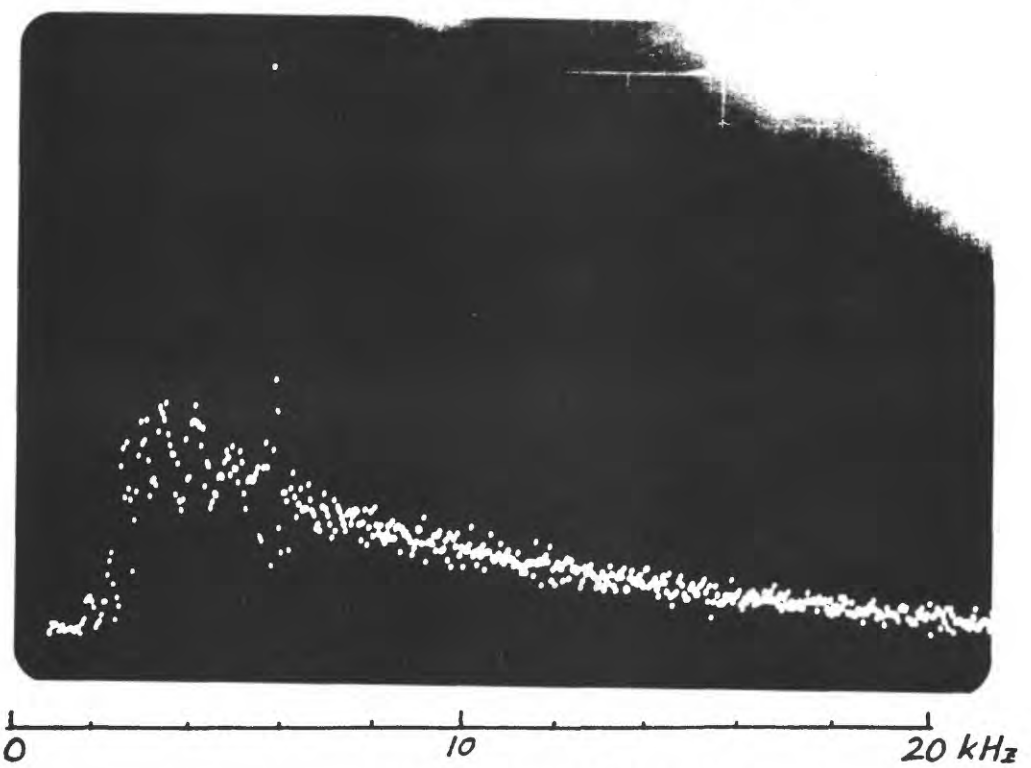

Spectrum

Fig. A6

Acoustic Emission Records

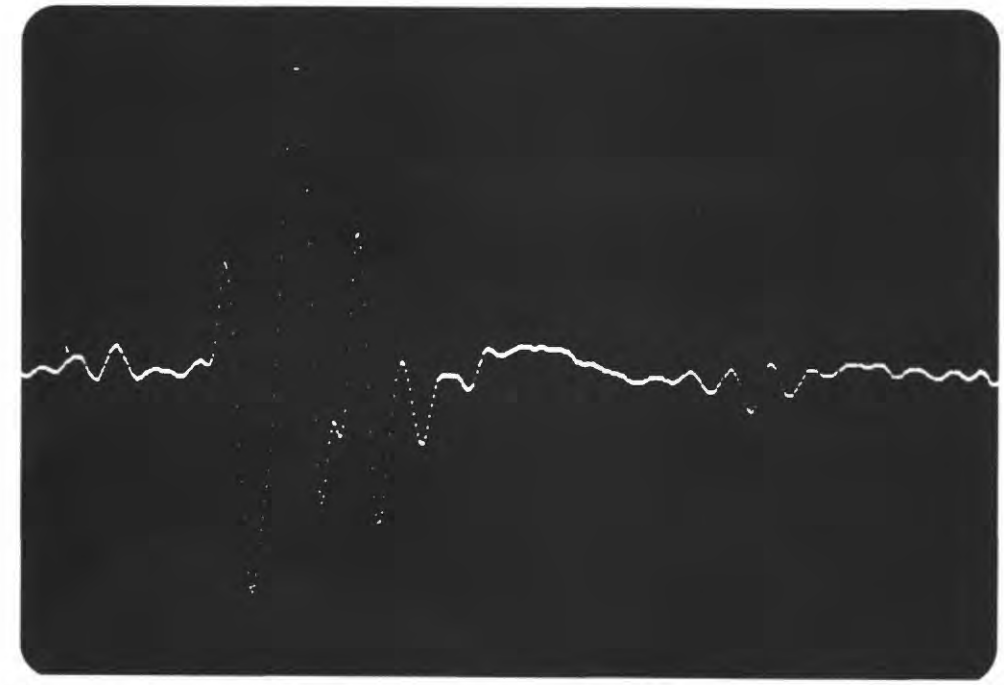

Time Function

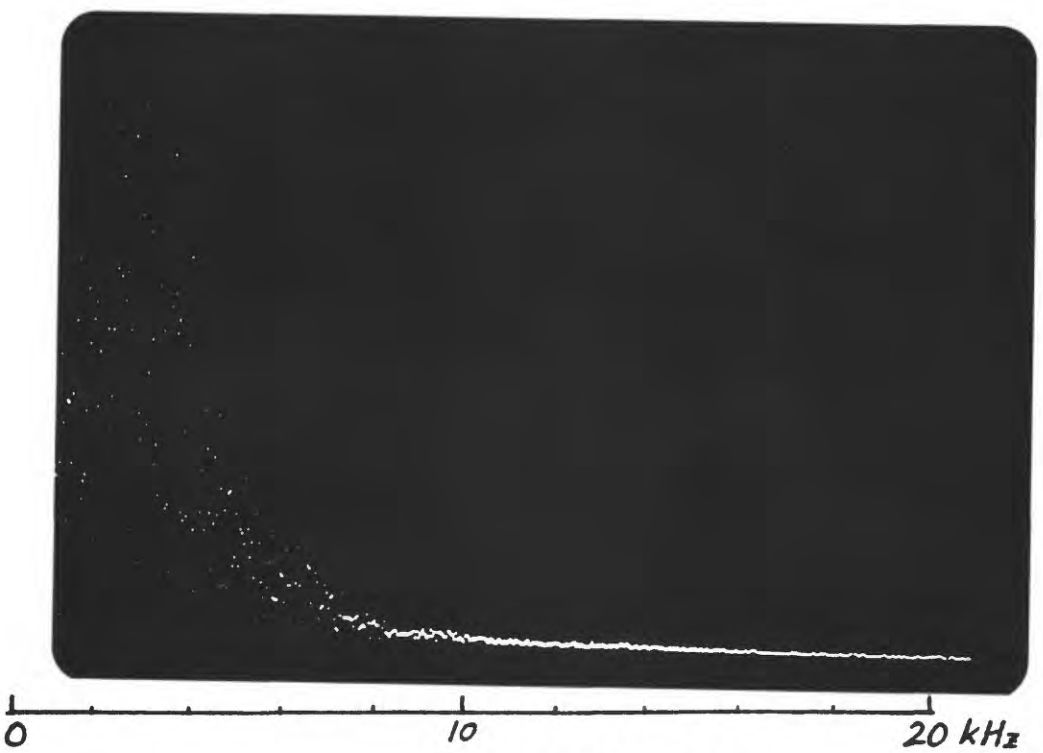

Spectrum

Fig. A7

Acoustic Emission Records

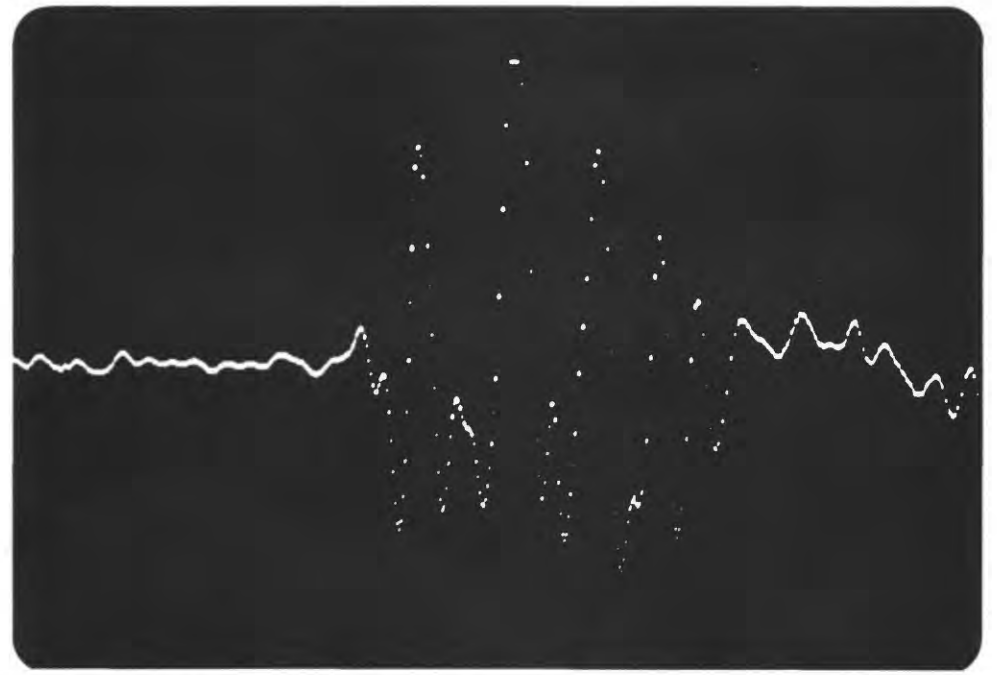

Time Function

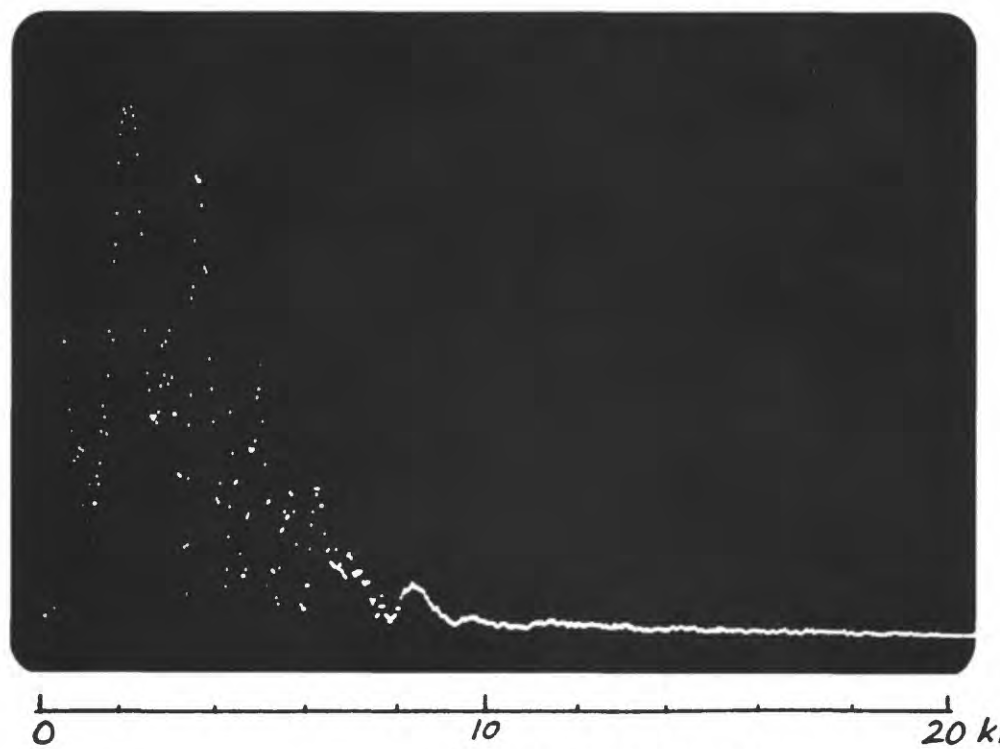

Spectrum

Fig. A8

Acoustic Emission Records

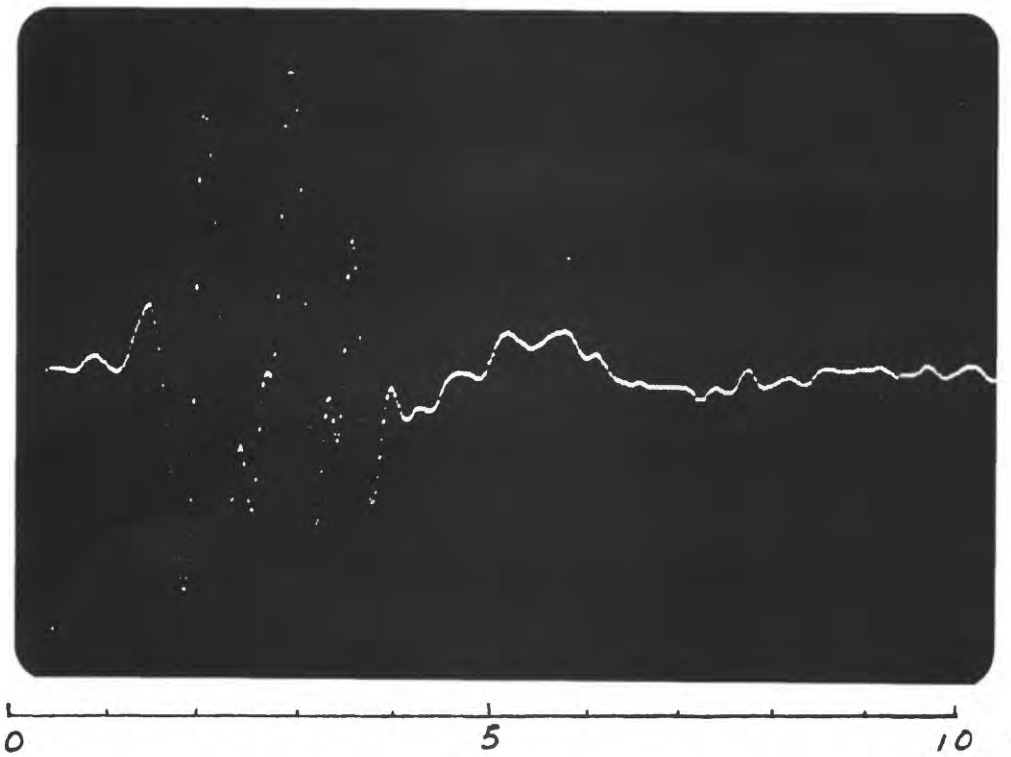

Time Function

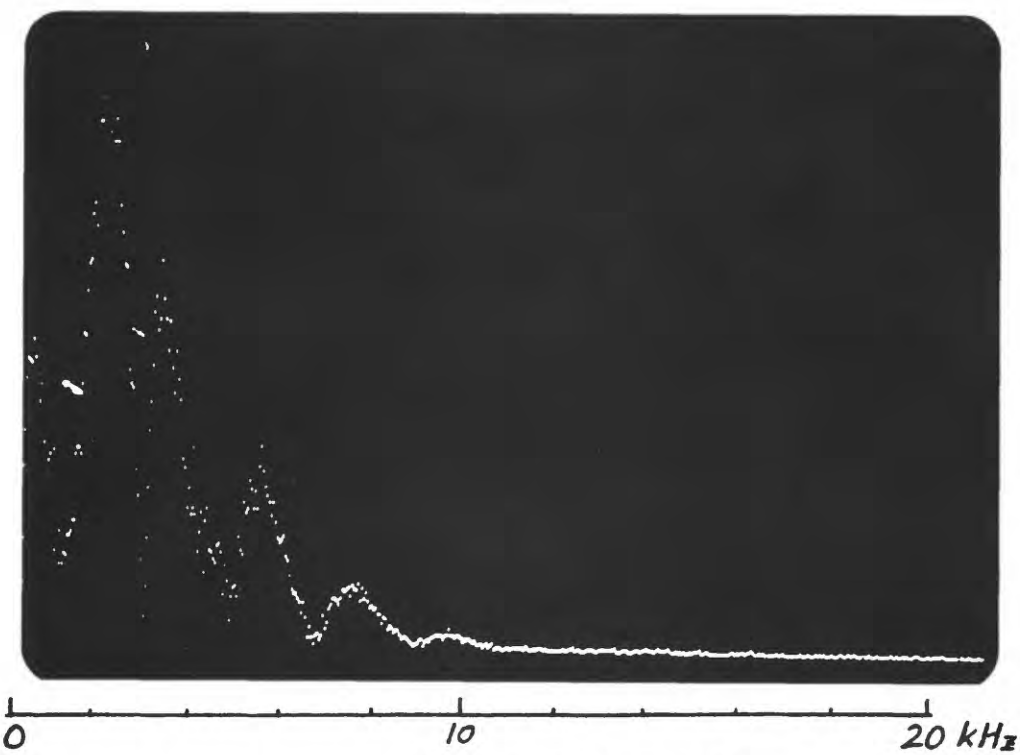

Spectrum

Fig. A9

Acoustic Emission Records

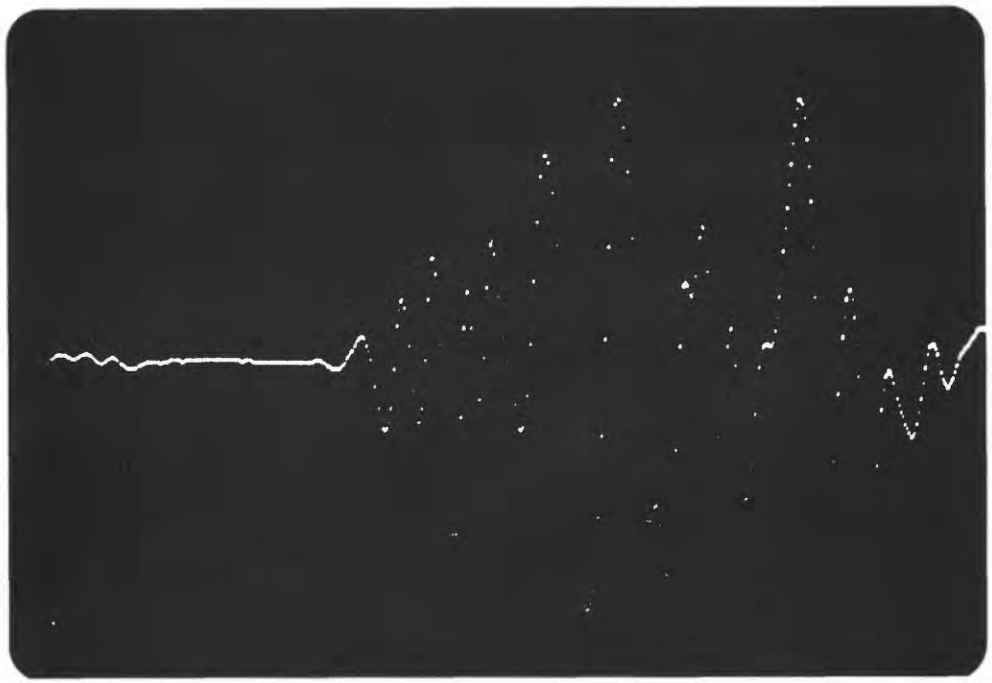

Time Function

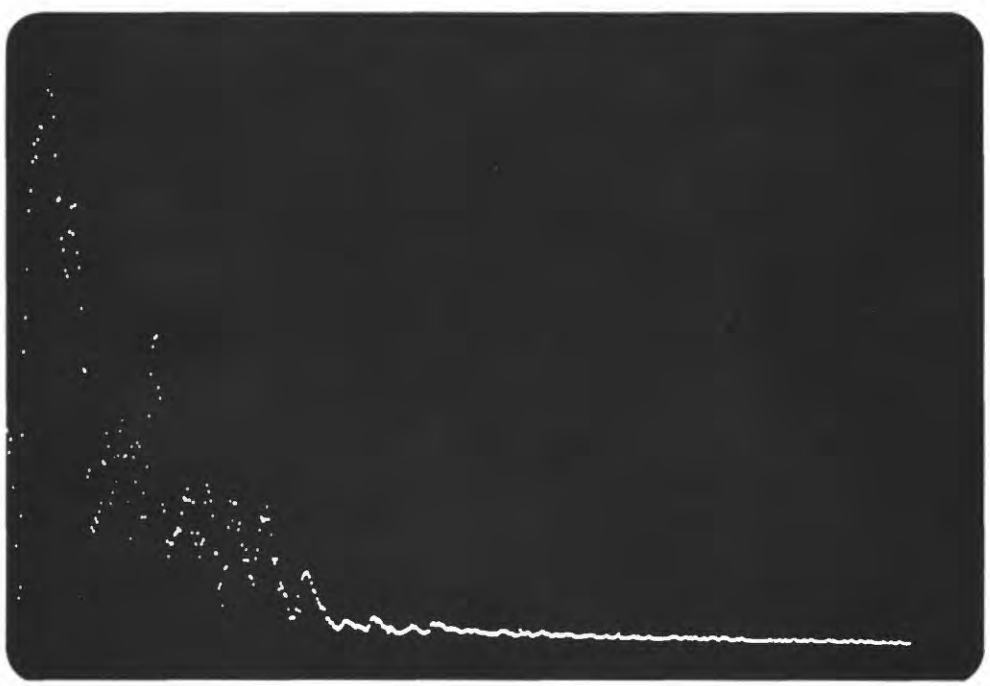

Spectrum

Fig. A10

Acoustic Emission Records

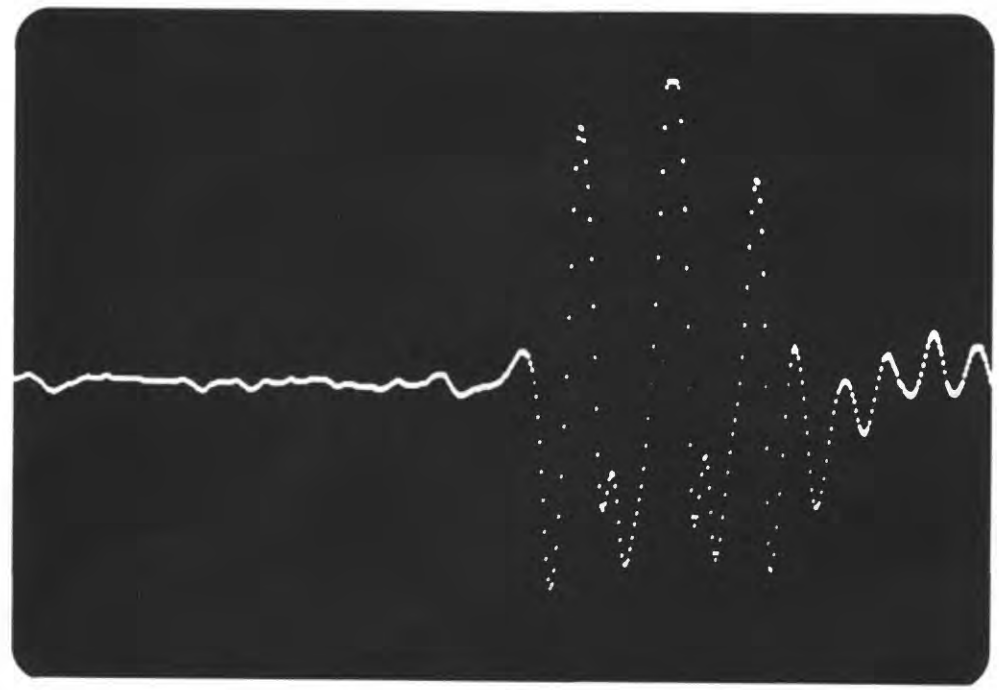

Time Function

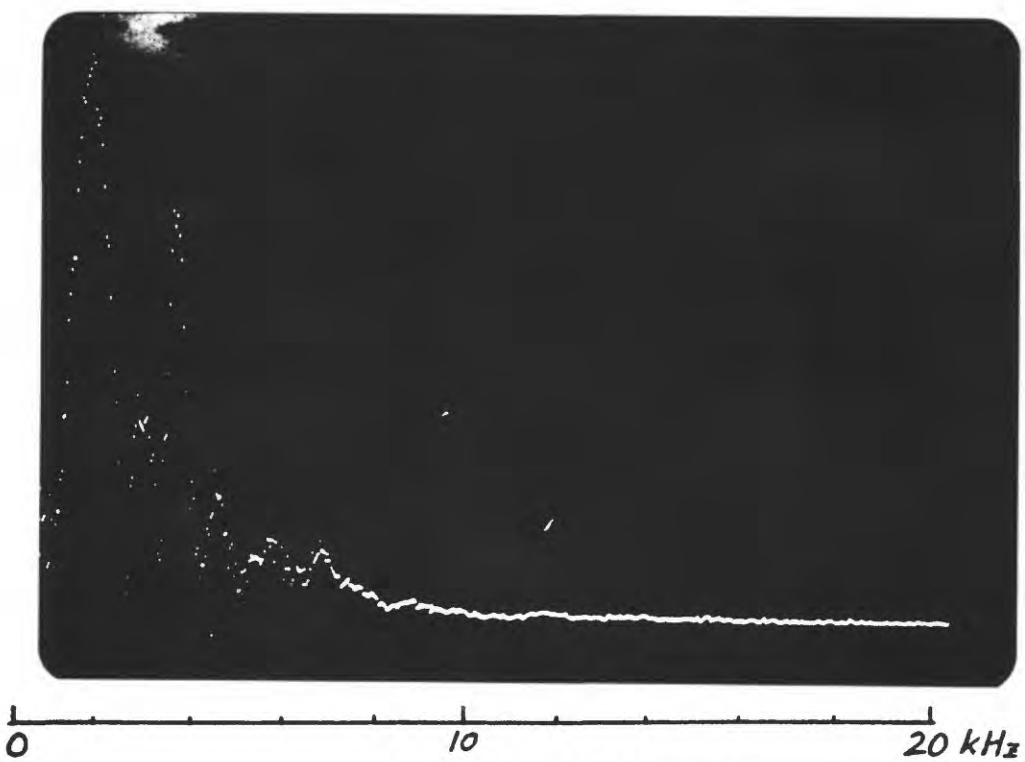

Spectrum

Fig. A 11

Acoustic Emission Records

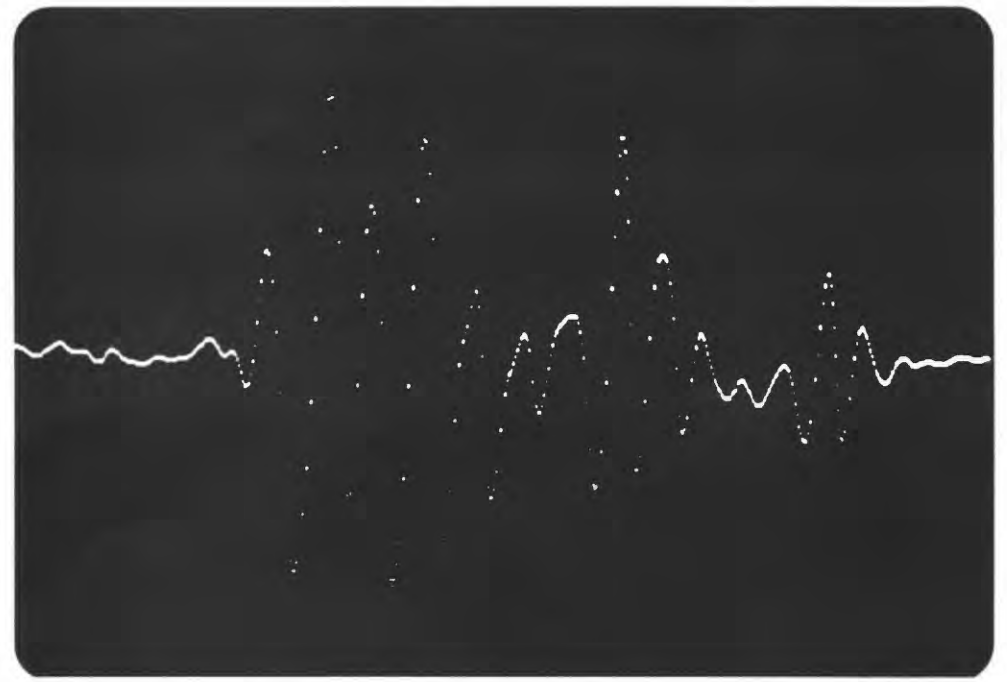

Time Function

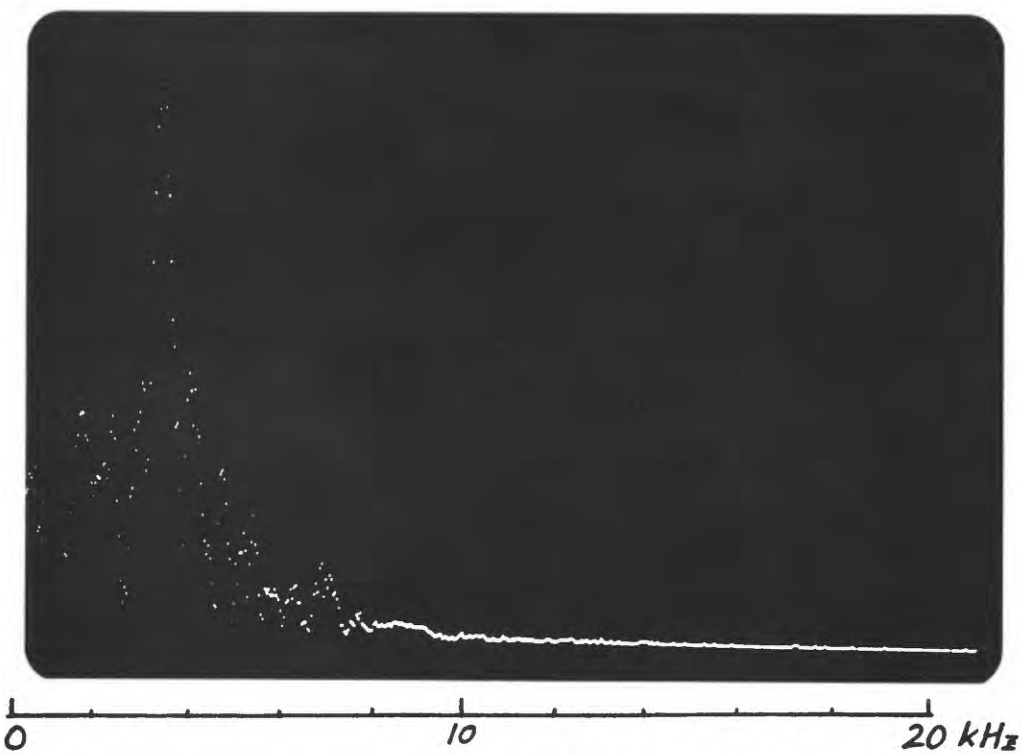

Spectrum

Fig. A12

ELECTROMAGNETIC EMISSIONS

Instruments have been constructed to detect potential electromagnetic (EM) emissions from the fracture or straining of quartz-bearing rocks. In addition to pre-seismic EM emissions, co-seismic emissions if detectable at reasonable distances from hypocenters can yield precise origin times for small events thus facilitating their accurate location.

Nitsan (1977) observed that EM energy was radiated during the fracture of quartz and quartz-bearing rocks in the laboratory, and suggested that they resulted from the rapid drop in the piezoelectric field accompanying the sudden release of stress when fracture occurs. Emissions were observed in the frequency range 1-10 MHz. There is little hope of detecting the MHZ signals in the field because of their rapid attenuation. We have, therefore, concentrated on frequencies well below 1 MHZ (bands centered at 100 kHz and 50 kHz), in the hope that faults in quartz-bearing rock will radiate EM energy most efficiently at wavelengths on the order of twice the fault length. Receivers which are deployed in deep boreholes minimize atmospheric RF noise and improve proximity to the source.

Our 100 KHZ RF receiver consists of a single wire antenna (350 foot) in series with a ferrite core antenna coil having a combined effective length of $\lambda/4$. The signal from the antenna is passed through two stages of of tuned, coupled RF amplification. The amplified signal is then rectified and integrated by an R.C. stage having a decay constant on the order of 0.1 sec. This integrated envelope of the RF signal is then sent to the surface and recorded on a strip-chart recorder. A block diagram of the receiver is given in Figure 7. Circuit diagrams are given in Figures 8 and 9. Ferrite antenna, amplifiers, detector, integrator, voltage regulator, and battery pack are housed in a 2 inch I.D. PVC pipe 81 inches long. The single wire antenna is attached to the lower end of the package (Figure 10).

BLOCK DIAGRAM R.F. RECEIVER

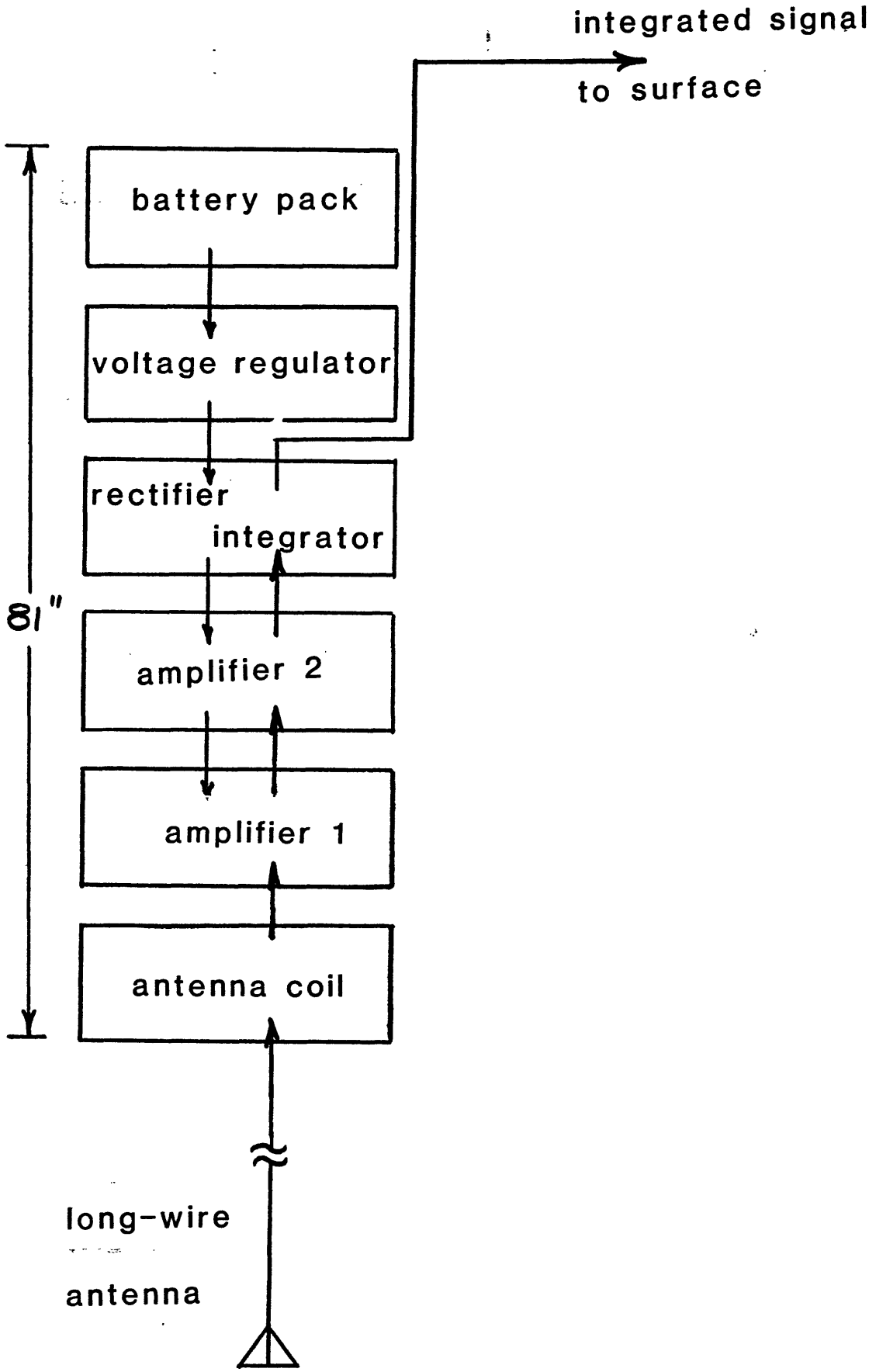

FIGURE 7

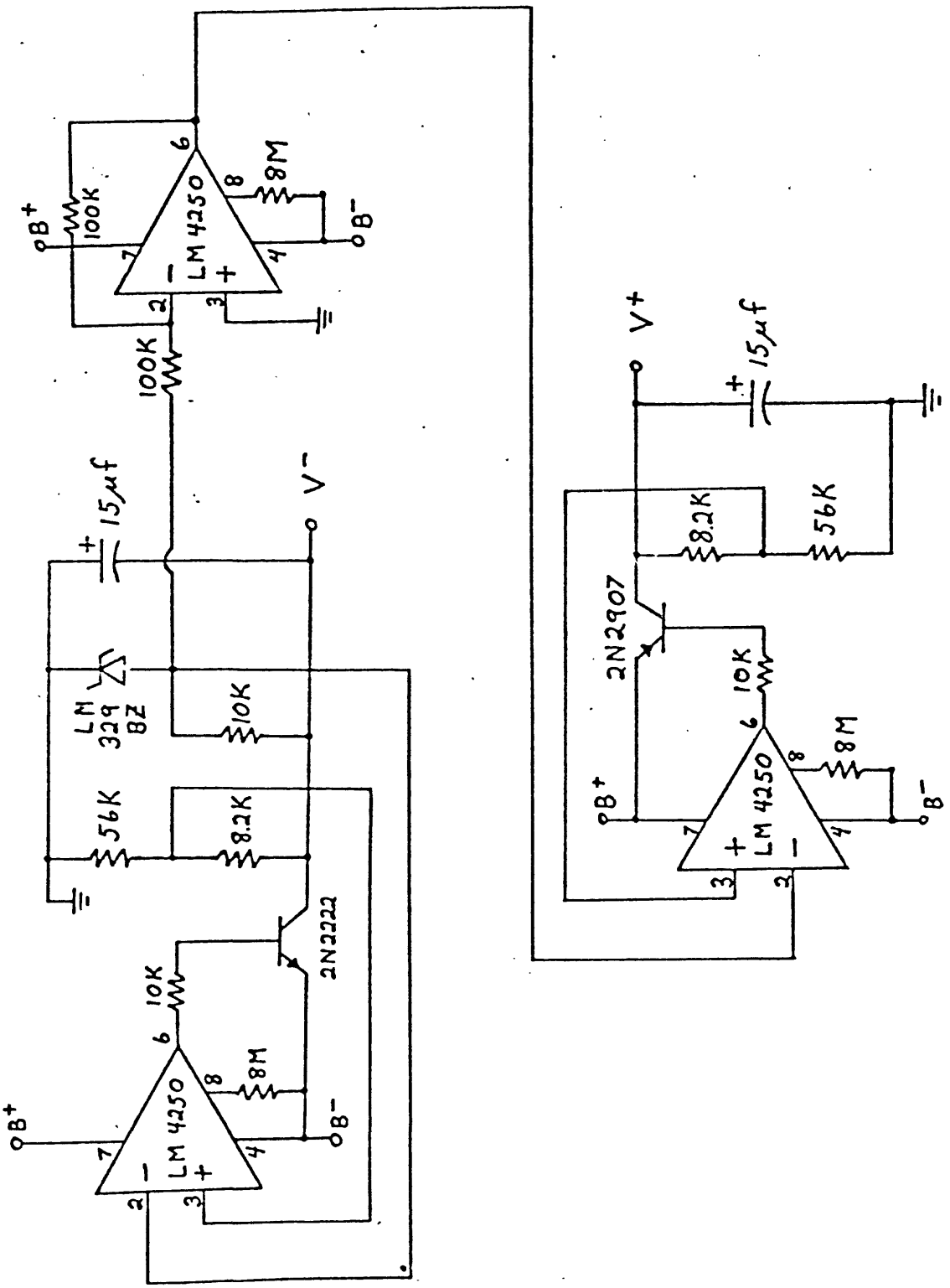

FIGURE 8
VOLTAGE REGULATOR/REFERENCE

CIRCUIT DIAGRAM R.F. RECEIVER

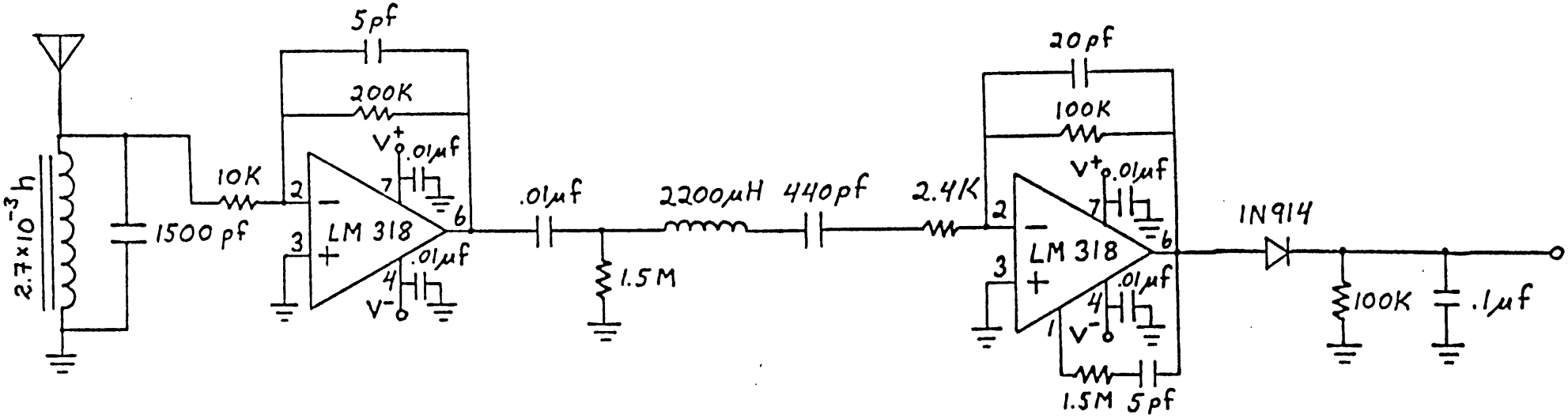

ANTENNA

AMPLIFIER 1

AMPLIFIER 2

RECTIFIER & INTEGRATOR

FIGURE 9

FIELD DEPLOYMENT

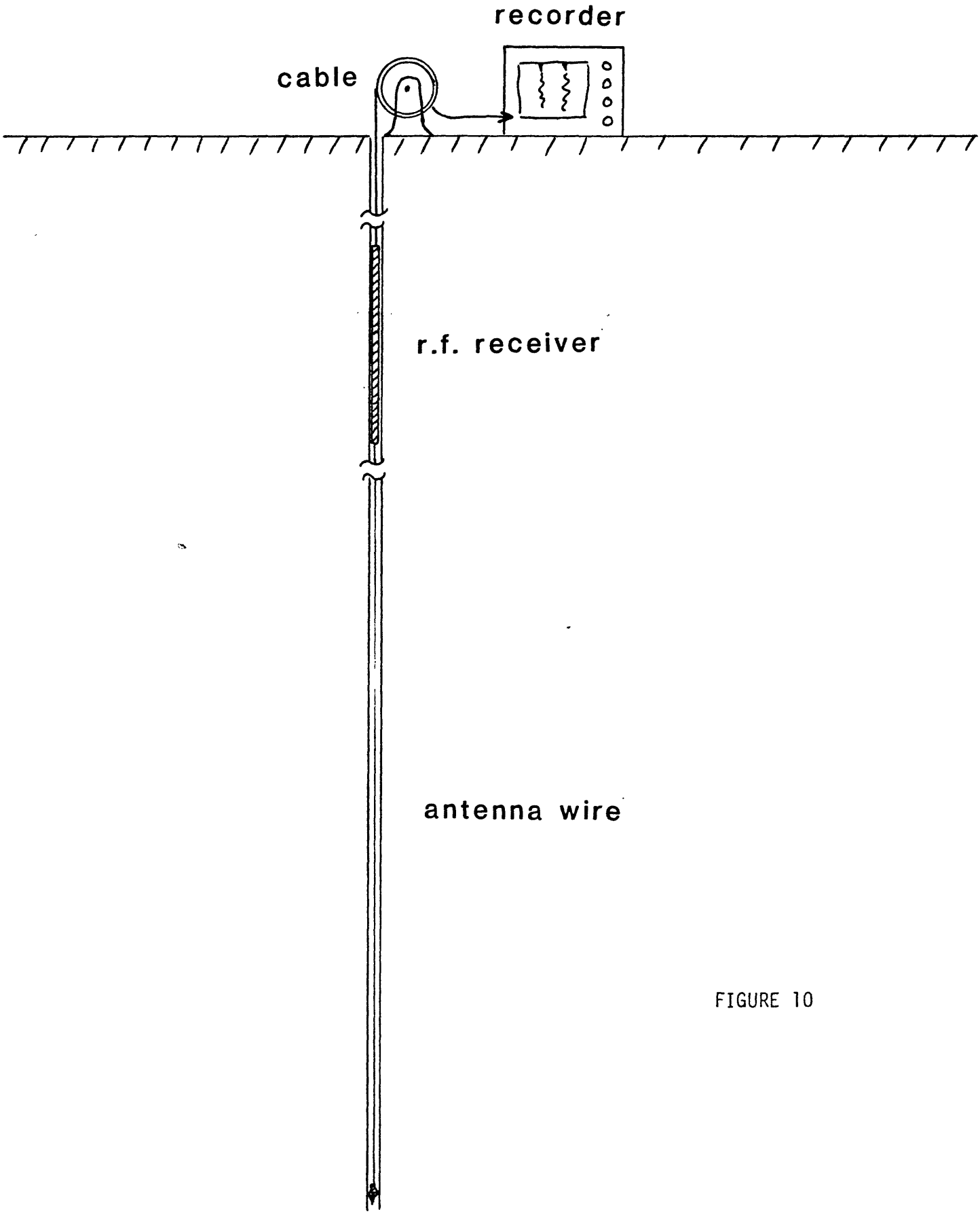

FIGURE 10

To date, the unit has been deployed in three of our uncased wells along the San Andreas fault (Haskell, Roberts, and Shandon Hills). In each hole, the background level was recorded as the instrument was lowered. The results are shown in Figure 11. We expect surface signals to fall-off as $\exp(-z/\delta)$ where the skin-depth δ is given by

$$\delta = (2/\mu w\sigma)^{1/2} \qquad (1)$$

and μ is the magnetic permeability and σ is the electrical conductivity. Typical values for rock are $\mu \sim 1.3 \times 10^{-6}$ henry/meter and $10^{-7} < \sigma < 10^{-1}$ mho/meter with $\sigma = 10^{-2}$ typical. At 100 KHZ, these values yield $5m < \delta < 5$ km. with $\delta = 16$ m. typical. It is interesting that in only the Roberts well did the background decrease as expected. At the other two wells the decrease is much slower. The interpretation of these results is complicated by the extremely long antenna (107m) and the presence of a water table. Shandon Hills is further complicated by side-hill topography.

More interesting results are the observation of transient events during two recent extended recording sessions. The first was at the Skelton well near Lancaster. A total of 41 hours of data were recorded between 5:00 p.m. Wednesday, November 7th and 10:00 a.m. Friday, November 9th as shown in Figure 12. The 100 KHZ receiver was operated at a gain of 200 at a depth of 500 ft. At the beginning of the record, a constant background is observed, but at approximately 8:00 p.m. (November 7) a series of transients are observed. They are irregularly spaced in time varying between 1/hr. and 5/hr. The amplitudes also vary irregularly. These transients continue until approximately 8:00 p.m. (November 8) when they become less and less frequent, dying out completely by 10:00 p.m. (November 8). No transients were observed during the remaining 12 hours of record.

A second set of transients were observed between January 22 and January 25 in the Roberts well (see Table I and Figure 1).

FIGURE 11

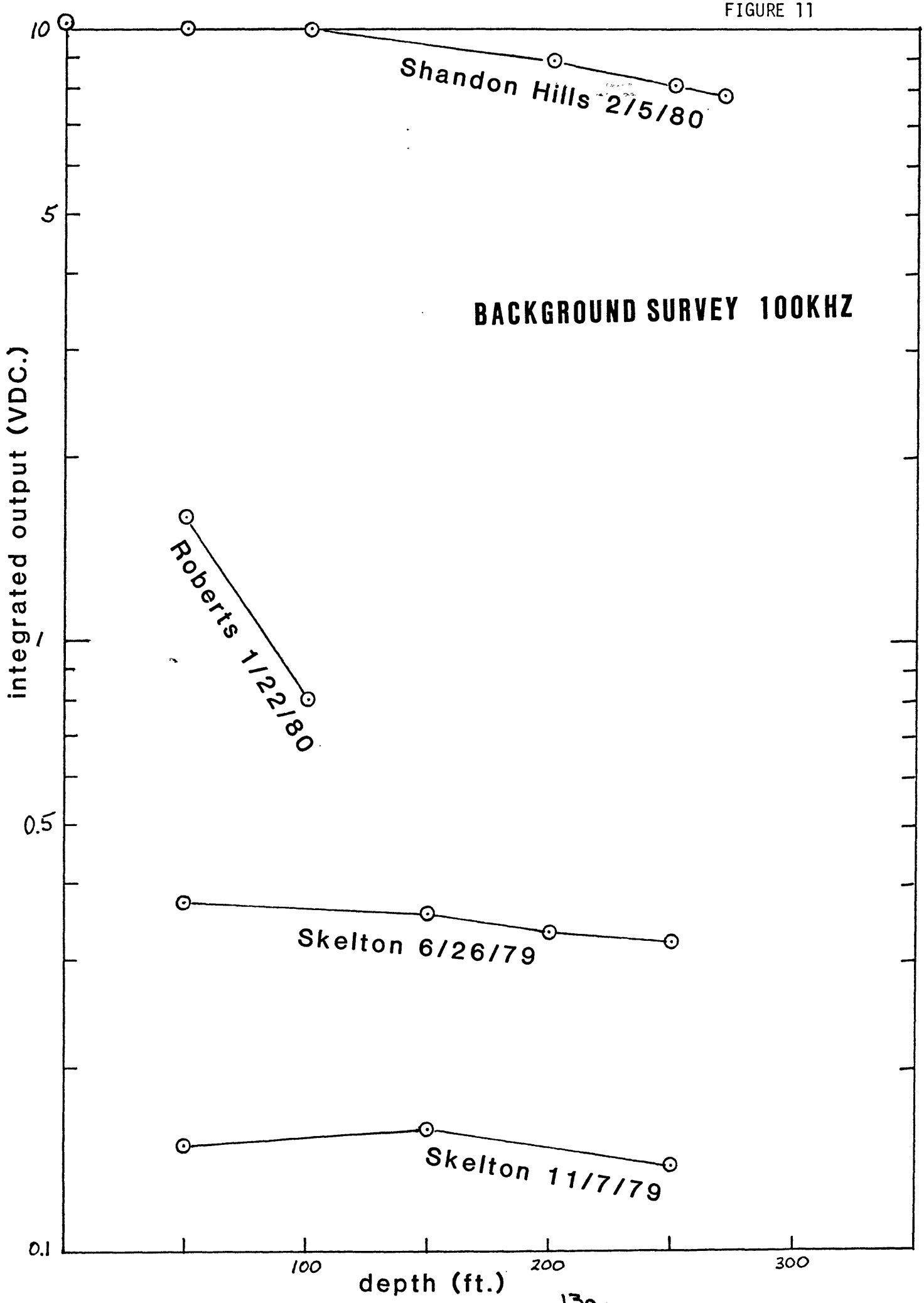
10
5
1
0.5
0.1
integrated output (VDC.)
BACKGROUND SURVEY 100KHZ
Shandon Hills 2/5/80
Roberts 1/22/80
Skelton 6/26/79
Skelton 11/7/79
100
200
300
depth (ft.)

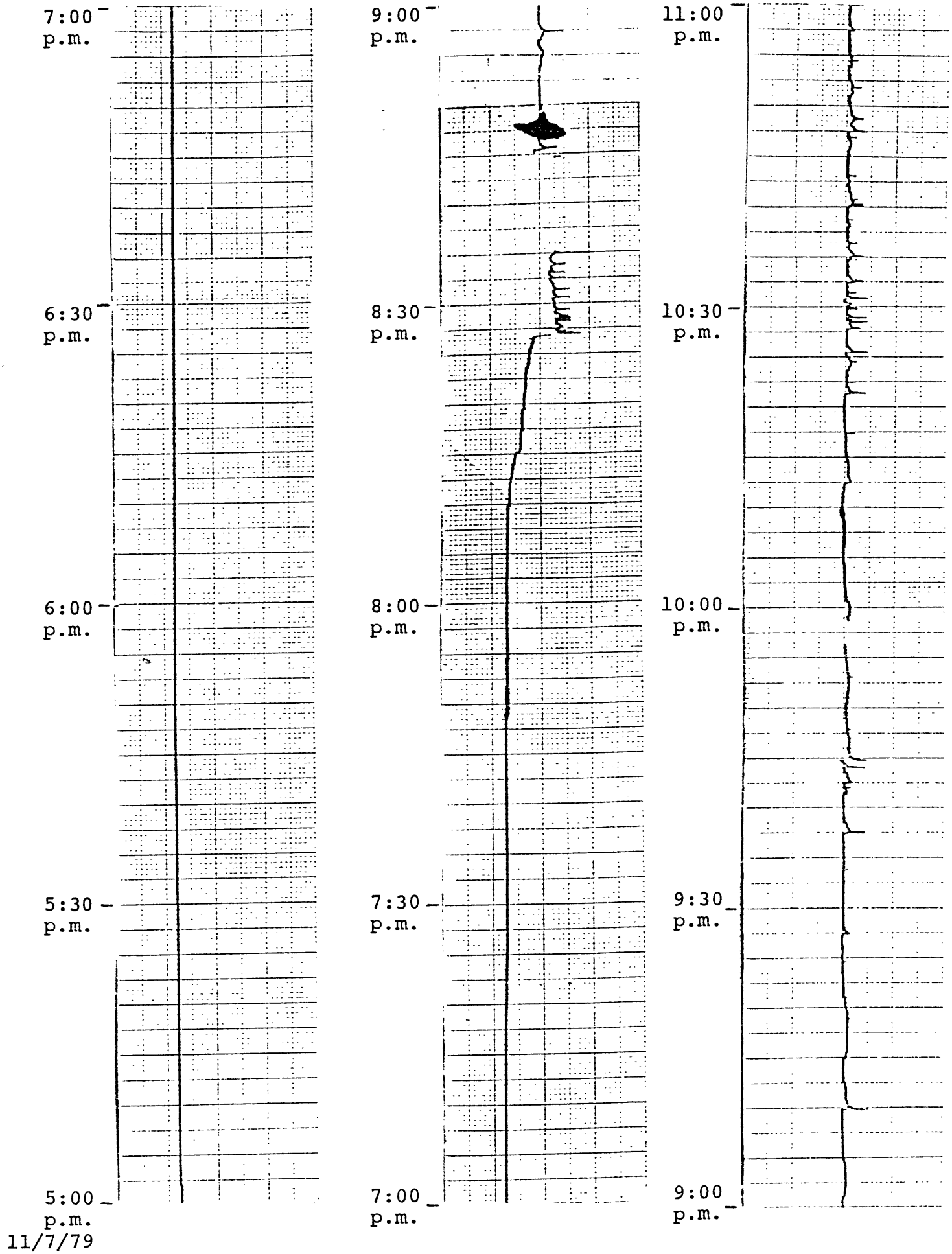

horizontal scale = .1V/cm

FIGURE 12

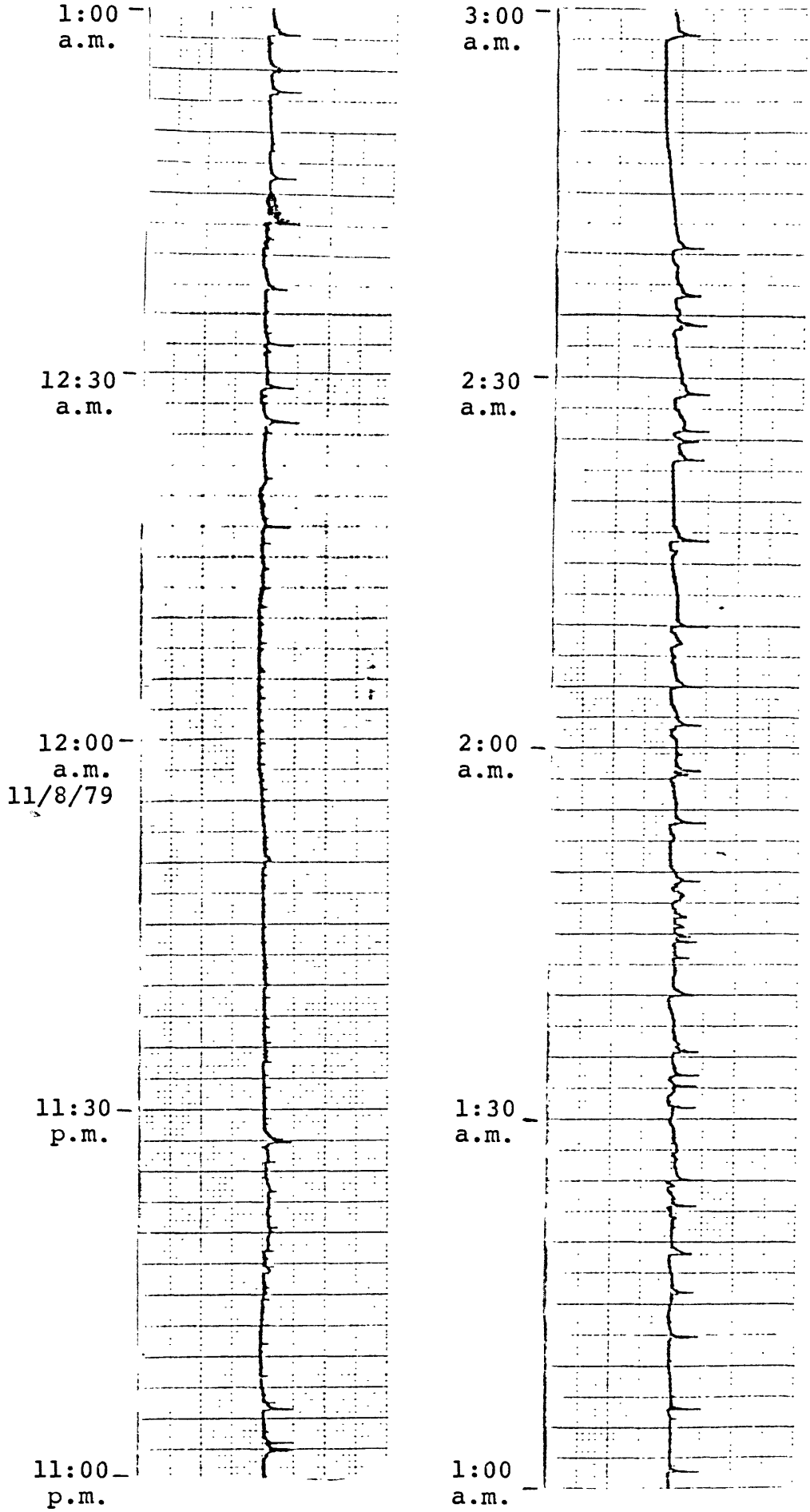

horizontal scale = .1V/cm

FIGURE 12 (Continued)

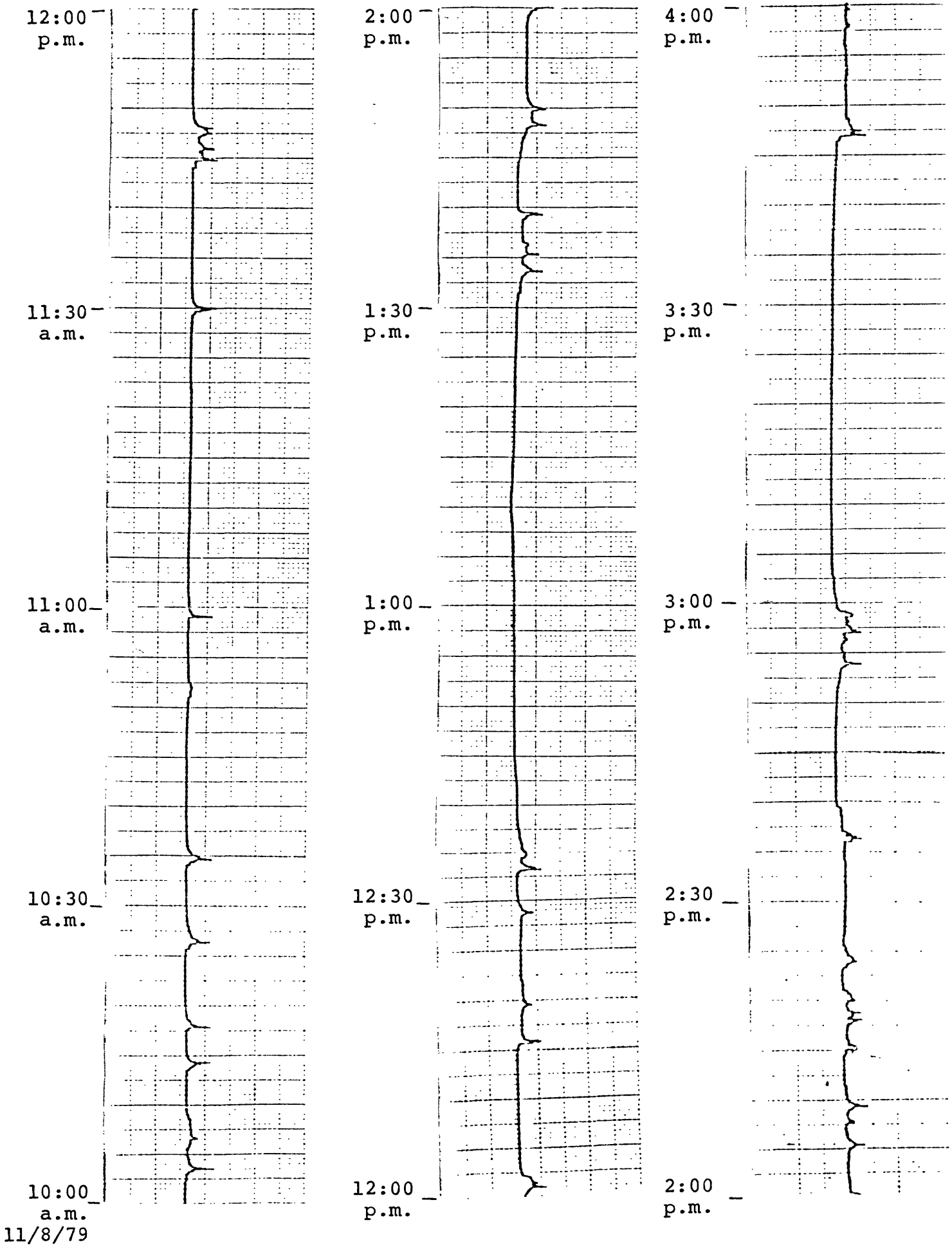

horizontal scale = .1V/cm

FIGURE 12 (Continued)

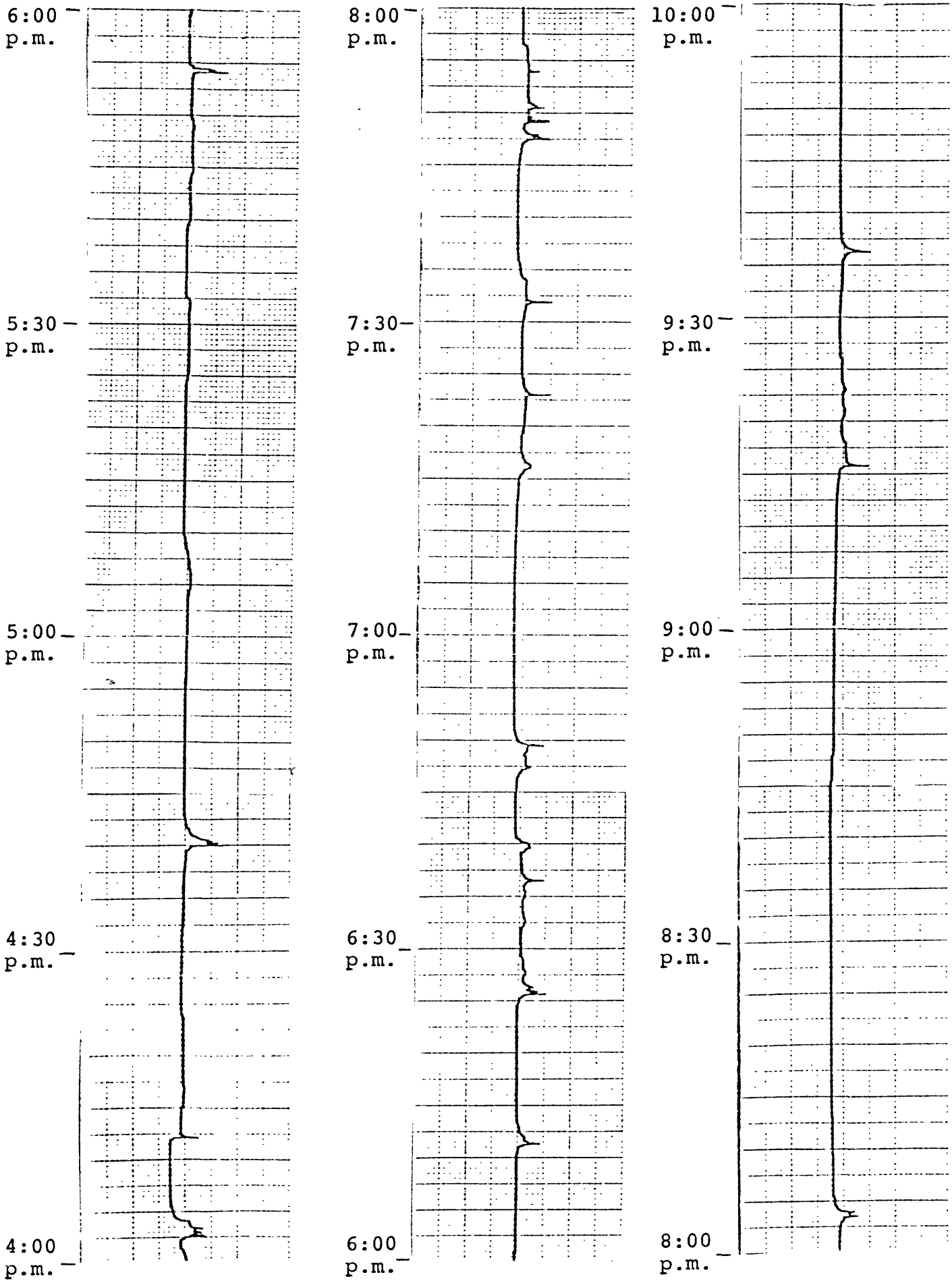

horizontal scale = .1V/cm

FIGURE 12 (Continued)

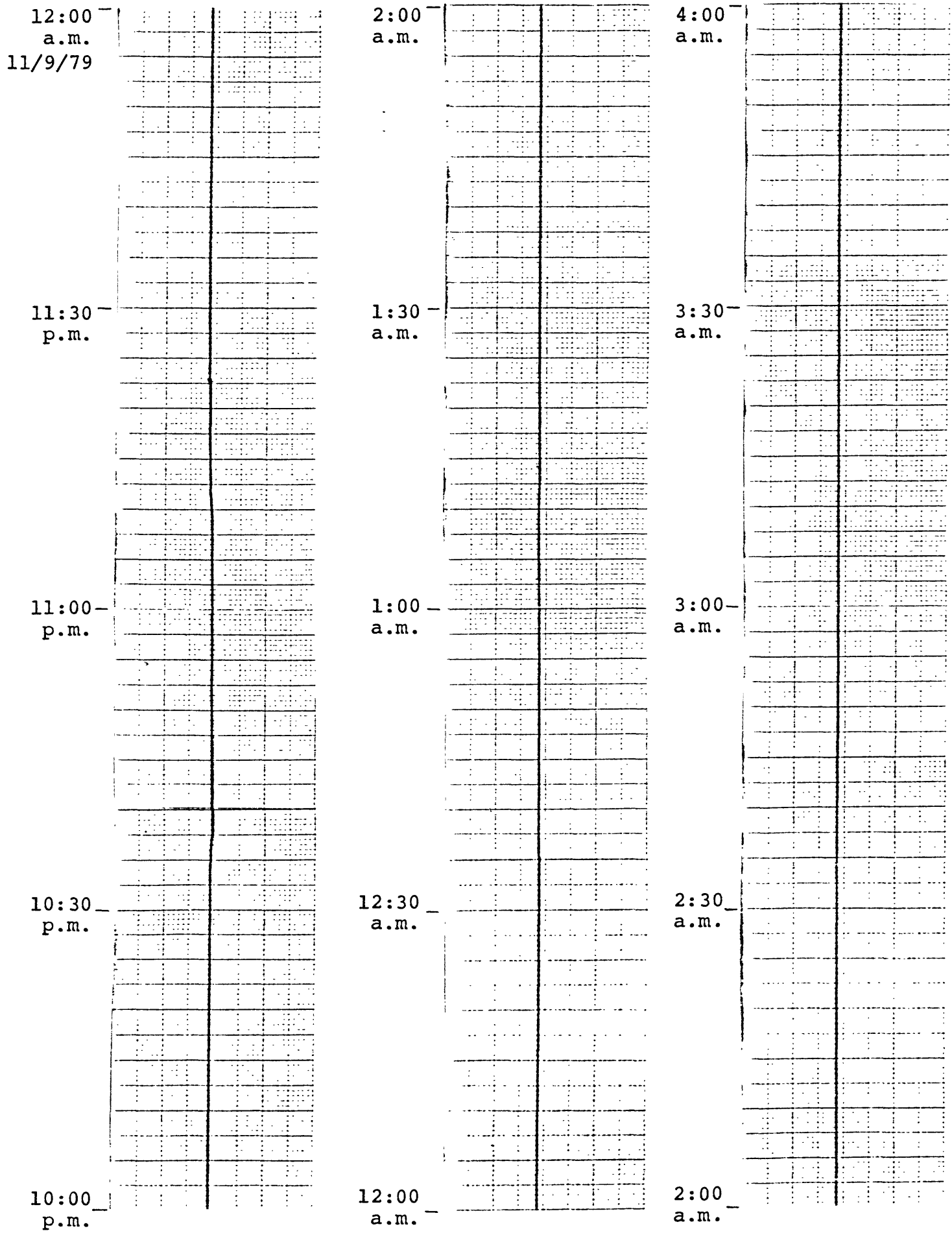

horizontal scale = .1V/cm

FIGURE 12 (Continued)

The 100 KHZ receiver was operated at a gain of 1000 at a depth of 100 feet. The record is shown in Figure 13. These transients differ from the previous set in their short duration and more frequent occurrence. As can be seen in Figure13a, they tend to occur in the early evening and early morning and are therefore probably cultural.

It may be significant that we have also observed high-frequency acoustic events at about the same occurrence rate in the same well (Skelton) as the first set of EM transients (Figure 11). Having developed, packaged, and field tested the E.M. receiver, a primary objective of the continuing work is to demonstrate a definite correlation between small seismic events and electromagnetic transients. At least two of these EM units will be deployed continuously in non-steel cased holes with acoustic emissions detectors. Unfortunately these units are not compatible with most other downhole instrumentation due to the downhole transmission of surface RF noise by these instrument's cables.

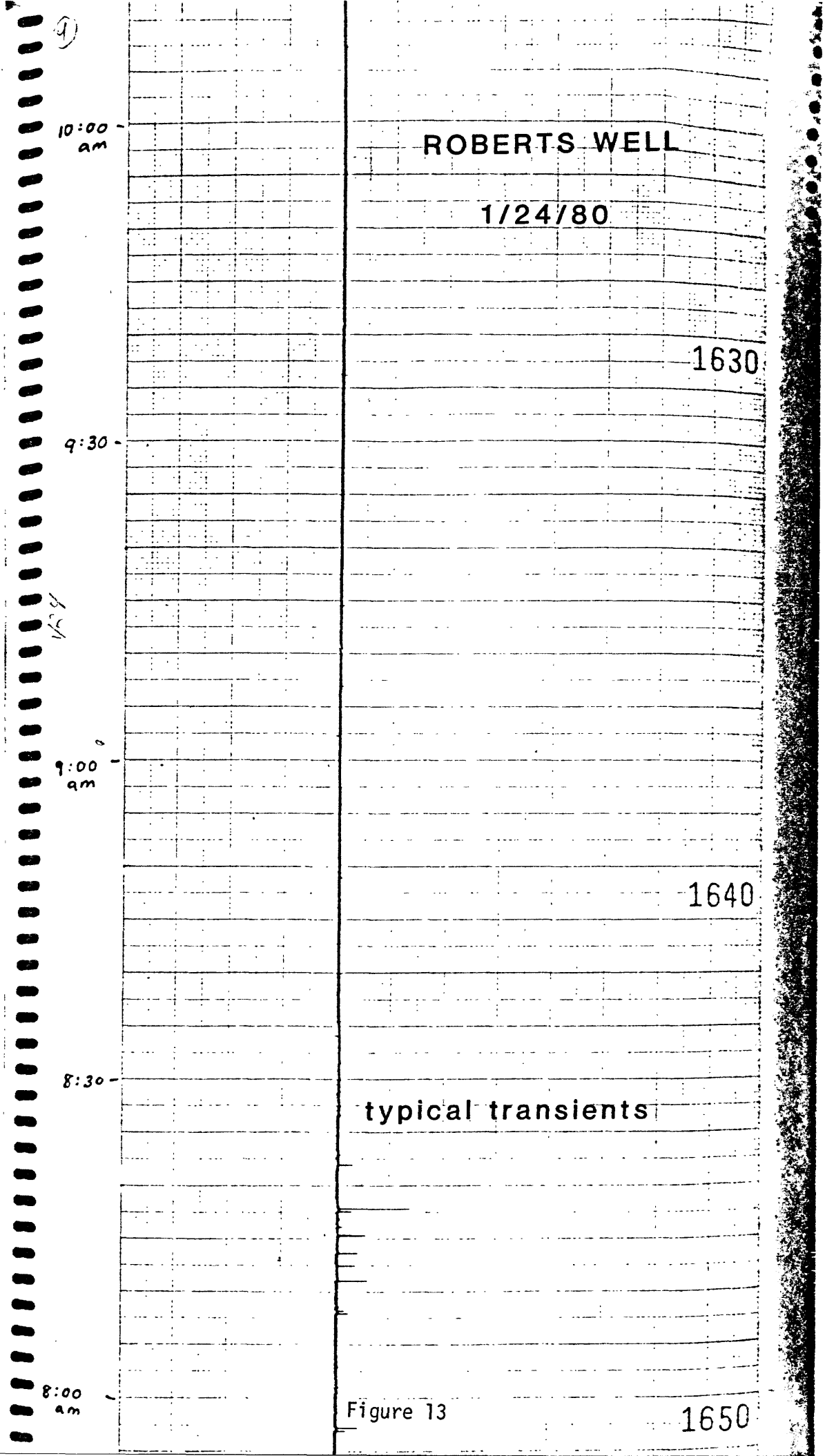
10:00 am
9:30
9:00 am
8:30
8:00 am
ROBERTS WELL
1/24/80
1630
1640
typical transients
1650

Figure 13

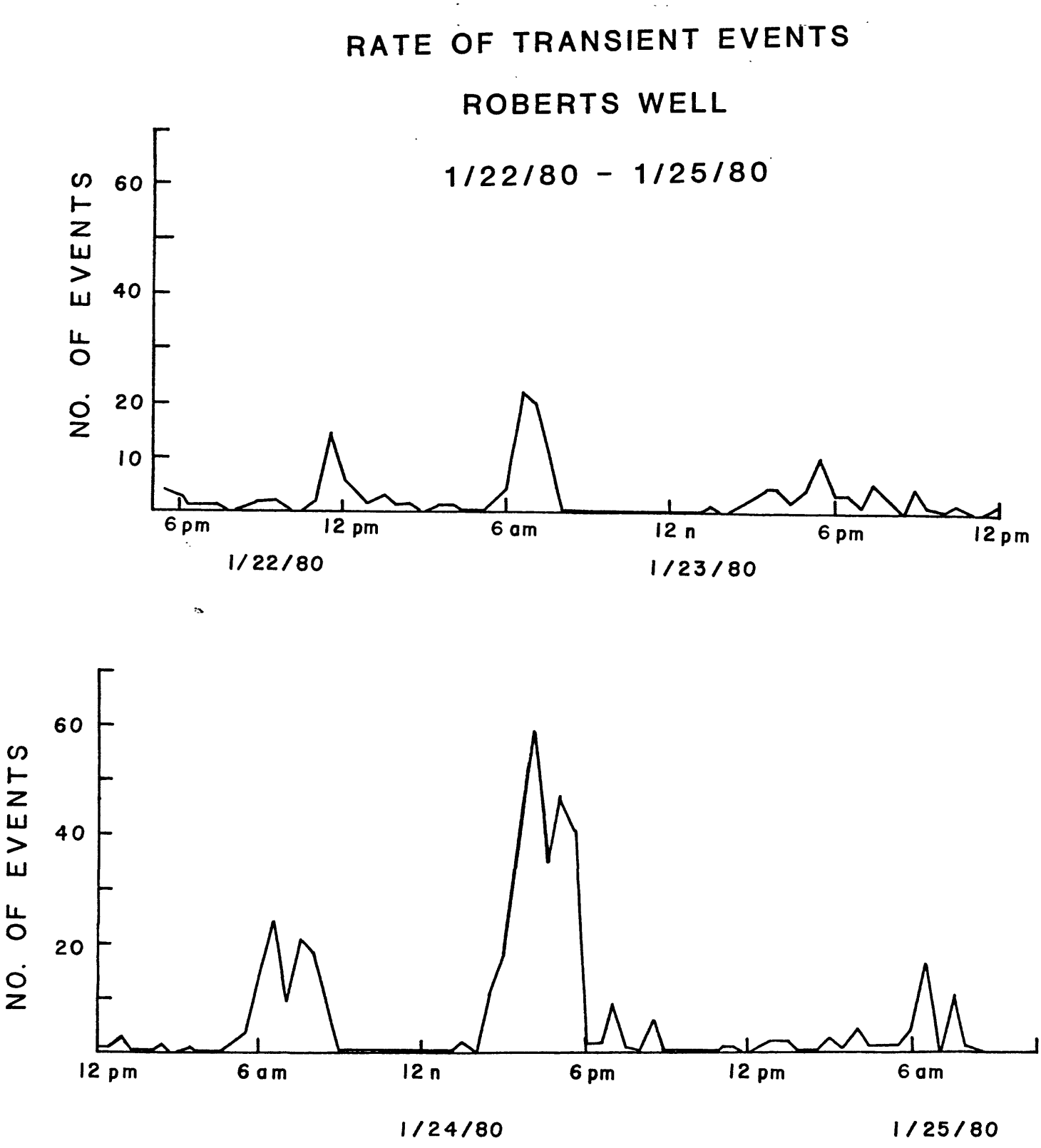
RATE OF TRANSIENT EVENTS
ROBERTS WELL
1/22/80 - 1/25/80
NO. OF EVENTS
60
40
20
10
6 pm
12 pm
6 am
12 n
6 pm
12 pm
1/22/80
1/23/80
NO. OF EVENTS
60
40
20
12 pm
6 am
12 n
6 pm
12 pm
6 am
1/24/80
1/25/80

FIGURE 13a

VECTOR MAGNETOMETER EXPERIMENT (Supplement to Deepwell program)

During the past year U.S.C. has been cooperating with U.C.L.A. in a comparative test of vector magnetometers for tectonomagnetic studies. We have been experimenting with a standard SHE corporation cryogenic magnetometer (for magnetotellurics), while U.C.L.A. is developing and testing a fluxgate. Work is being carried on at the JPL magnetometer station in San Gabriel Canyon northeast of Pasadena. Last year, in a "shakedown test" we ran a single 3-axis SHE cryogenic magnetometer in conjunction with a U.C.L.A. "stand-in" fluxgate. This permitted us to identify the requirements for a "serious" comparative test.

We discovered that flux-jumping on the cryogenic instrument and the need for a digital data format necessitated a specially constructed multi-channel recording interface which was designed by SHE engineers and constructed at U.S.C. during the fall of 1979. With completion of this unit and the final U.C.L.A. fluxgates a second comparative test was begun about two weeks ago. We have just installed two 3 component cryogenic magnetometers, together with a bubble tiltmeter, on a marble slab in a 6 foot deep vault at San Gabriel. The U.C.L.A. magnetometer is about 10 meters away in an insulated surface vault.

The first comparative data between the two cryogenics for the near-vertical and one near-horizontal axes are shown in Figures 14 and 15 (Note respective components are 180^0 out of phase for display). No comparisons have yet been made with the U.C.L.A. fluxgate. This test run will continue for approximately 4 weeks. Figures 14 and 15 indicate the two cryogenics are tracking well as evidenced by both the similarity in curve slopes and the stability of the crossing points of the mirror image curves ($\pm 2\gamma$ over 48 hours). The relative differences in amplitude are attributed to non-parallelism of the respective X and Z components and a small difference in calibration which has not yet been factored out. Parallelism of the magnetometers has only been done

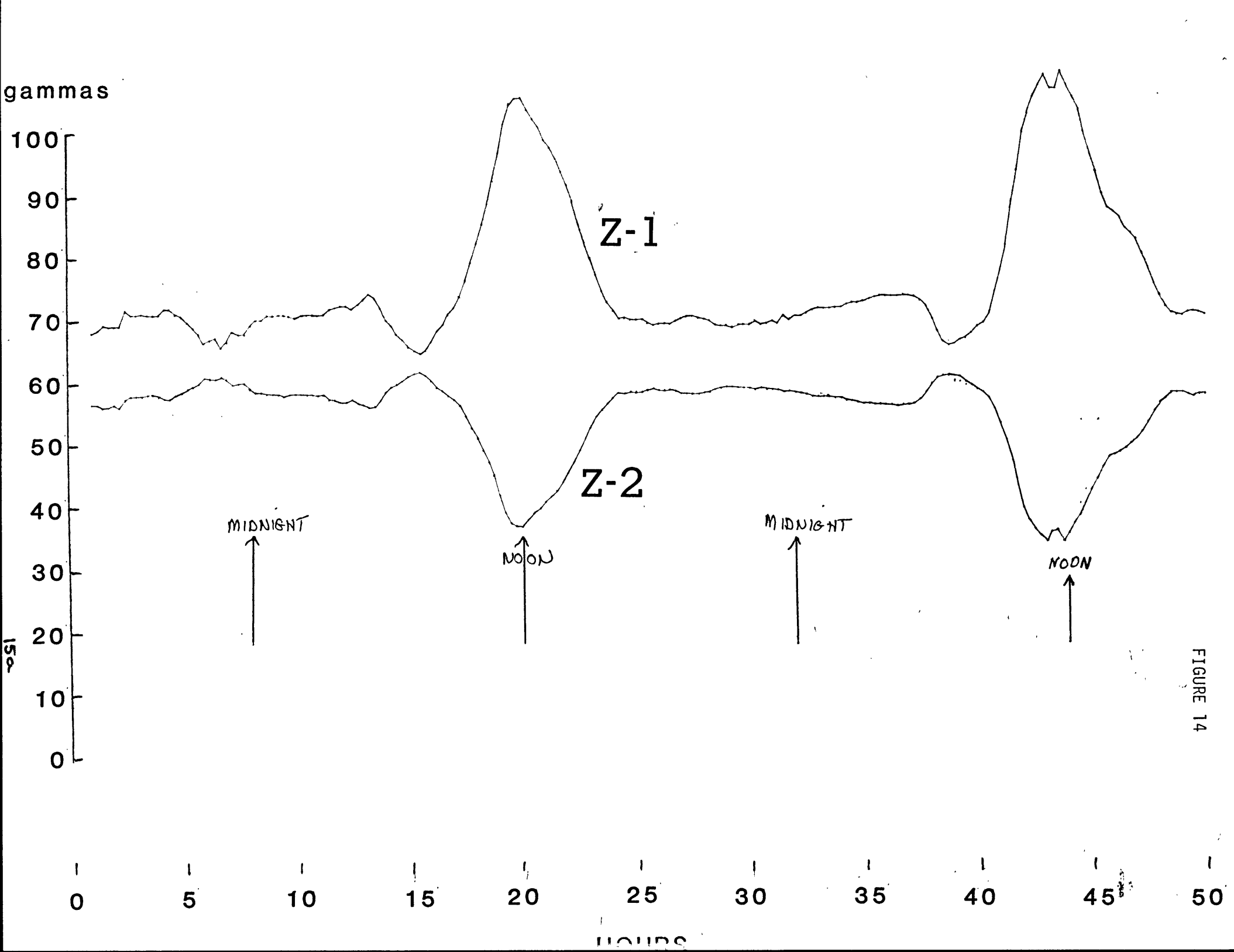
gammas
100
90
80
70
60
50
40
30
20
10
0
Z-1
Z-2
MIDNIGHT
NOON
MIDNIGHT
NOON
0
5
10
15
20
25
30
35
40
45
50
HOURS

FIGURE 14

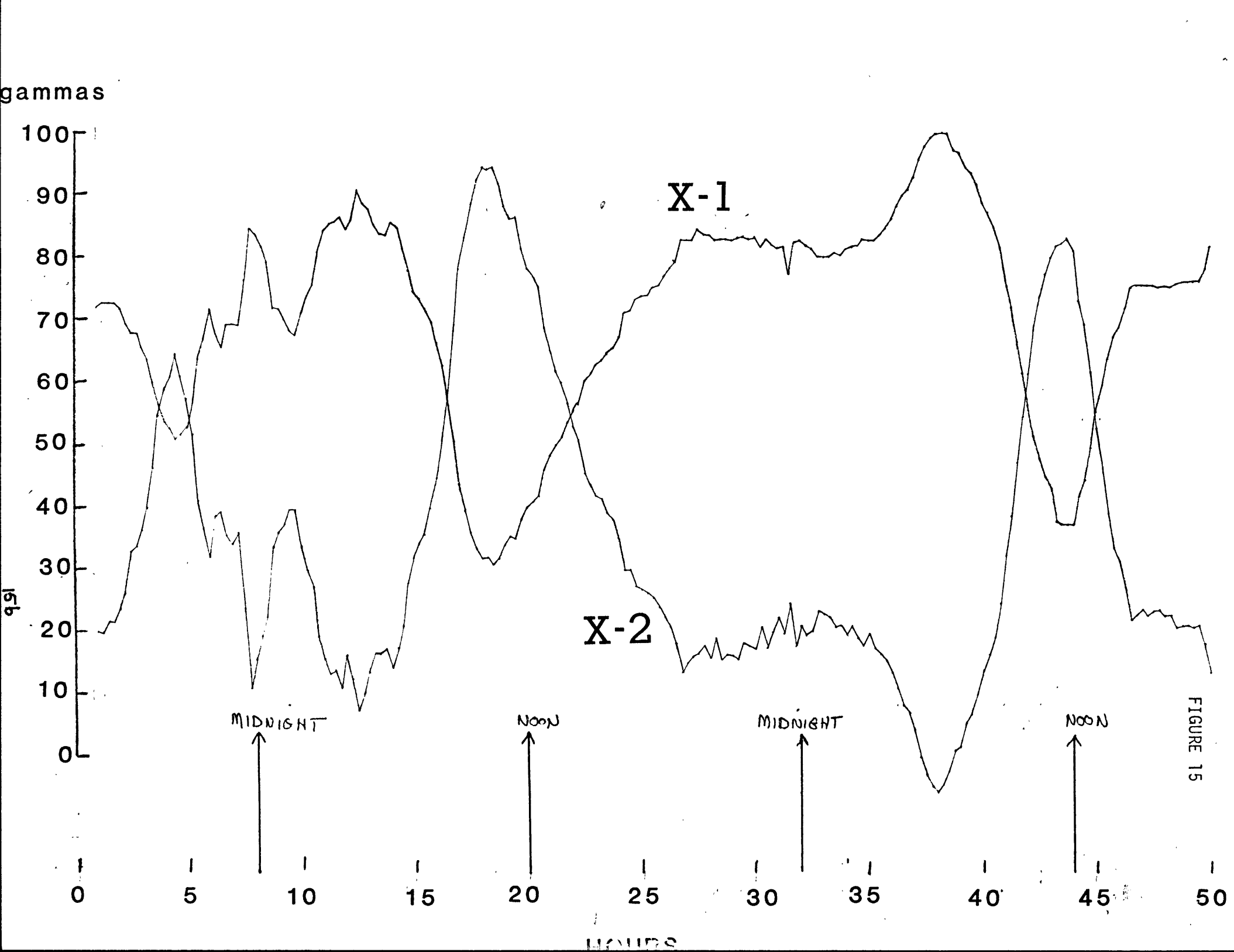
gammas
100
90
80
70
60
50
40
30
20
10
0
X-1
X-2
MIDNIGHT
NOON
MIDNIGHT
NOON
0
5
10
15
20
25
30
35
40
45
50
HOURS

FIGURE 15

to-date by eye; perfect alignment of the external cases, however, would only ensure at best a $\pm 1/2^0$ alignment precision per the manufacturers specifications. The $\pm 2\gamma$ variability at crossing points can be attributed to small H-field rotations acting on non-parallel axes, and need not be due magnetometer instabilities. Thus it will be necessary to determine the stability of the linear dependence of individual components of one magnetometer on the components of the other magnetometer. Relationships of this kind will also be investigated between the cryogenics and fluxgate.

WATER LEVEL-TURBIDITY-TEMPERATURE PACKAGE

The sensors for this package have given numerous problems as we have reported earlier. However, with the acquisition of new pressure transducers (Paroscientific Digiquartz), an improved photocell design for the turbidimeter, and specially constructed cable termination - high pressure feedthrus, the sensors (Figures 16 and 17) are all currently ready for permanent deployment. Cable delivery is expected during February, 1980; it has been delayed in the fabrication process about five months by the manufacturer (Rochester Cable).

Our decision to switch from the standard strain gage pressure transducer to the Digiquartz to achieve long term stability (now better than 1 mm of H_2O over $\sim$ 1 month) also necessitated the design and construction of a frequency-to-analog voltage interface for continuous recording.

Field deployment of the level detector, turbidimeter and thermal sensors at the earliest data has been given top priority.

Turbidimeter

Fig. 16

Pressure Transducer

Thermal Gradiometer

Fig. 17

WELL PERMEABILITY

Some of U.S.C.'s downhole experiments are based on the following two important (and somewhat related) premises:

(1) sufficient permeability exists in the local formation such that water can serve as a means of communication of stress-induced information.

(2) ground water communication can in fact occur between hole and formation. Whether or not it does occur is also clearly important. Additionally, dilatancy (which may occur in or near a fault zone) implies an increase in permeability (given interconnecting microcracks or pores) with time.

Thus we have assembled the necessary equipment to make measurements in our deep wells, using standard well drawdown and recovery techniques. This includes a winch operated submersible pump having an 800 gph capacity at 1000 ft. depth, and powered by a 12 kw generator. A 1500 psi Digiquartz pressure transducer will monitor recovery and a thermistor probe lowered from our logging winch will be used to construct pre and post-recovery thermal profiles of the hole to investigate zones of recharge.

Figure 18 shows a typical drawdown and recovery curve for the case of radial flow in a confined aquifer at depth bounded by two horizontal planes. For this simple case, the permeability k, or, more commonly the transmissibility, T (defined as the rate of flow in gallons per day through a vertical section of the aquifer whose height is the thickness of the aquifer and whose width is one-foot when the hydraulic gradient is 1.00) is related to the depressed depth (at the well) from the static water level by the equation:

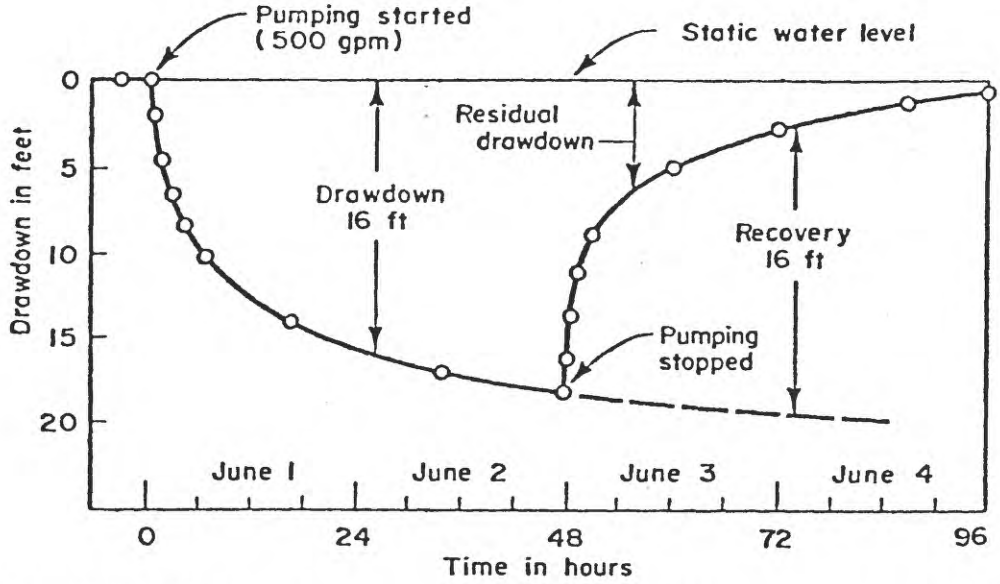

Figure 95. Typical drawdown and recovery curves for a well pumped for 48 hours at a constant rate of 500 gpm followed by idle period for water-level recovery.

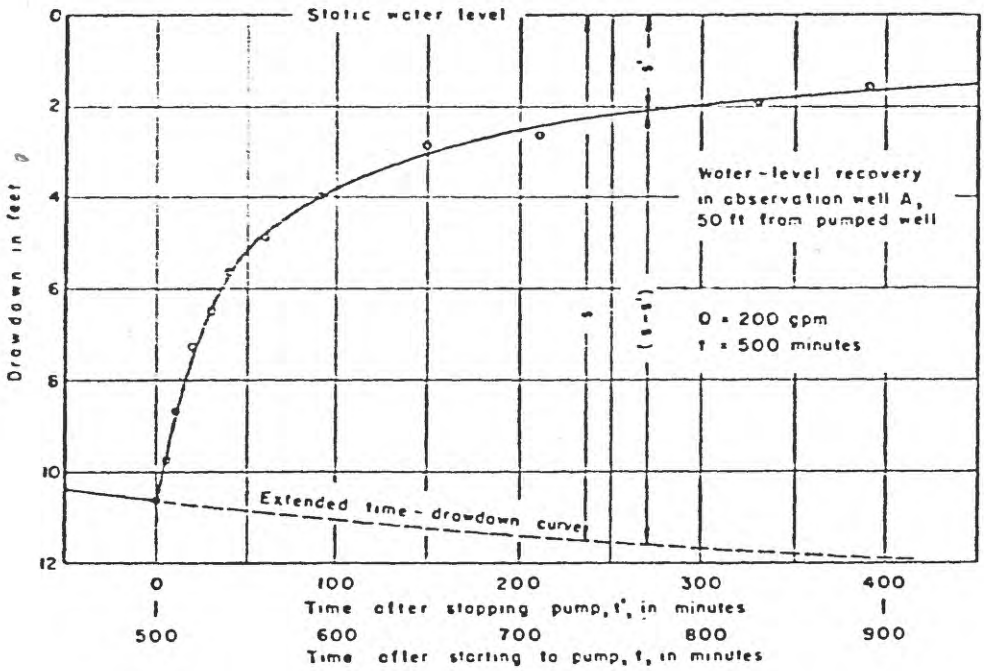

Figure 97. Residual-drawdown curve from observation well A, with extended time-drawdown curve, on arithmetic scales, showing how calculated recovery is determined at any instant during the recovery period. Producing well pumped at 200 gpm for 500 minutes.

FIGURE 18

*From Groundwater and Wells, Universal Oil Products Company St. Paul, Minnesota, 1972.

$$S' = \frac{264Q}{T} \log \frac{t}{t'} \qquad (1)$$

where: S = depressed depth (residual drawdown)

Q = discharge rate during pumpdown in gal/min.

t = time after pumping started in minutes

t'= time after pumping stopped in minutes

T = coefficient of transmissibility in gal/day/ft.

defined as T = Kb.

b = aquifer thickness in ft.

K = hydraulic conductivity in gal/day/ft^2

defined as $K = \frac{kg}{\nu}$

k = permeability in ft^2

g = gravitational acceleration in ft/sec^2

ν = kinematic viscosity in ft^2/sec

A plot of s' as a function of $\log \frac{t}{t'}$, yields T and hence the permeability, k, as shown in Figure 19.

The case of a leaky artesian aquifer may also be treated analytically (see eg. Davis and DeWiest, 1966, Chapter 7), the rate of leakage is determined by the magnitude of the deviation of the observed residual drawdown, s', from that predicted for the confined aquifer by (1).

More complicated cases such as multilayer aquifers and flow situations having a significant vertical (z) component of flow are easily modeled using two-dimensional (r, z) finite element or finite difference numerical techniques. A finite difference code for modeling fluid flow, heat transport, and hydrothermal reactions in a geothermal reservoir (Sammis, 1976) has been simplified to model the drawdown and recovery for the subsurface geology appropriate to each of our wells. Such models will give us a detailed picture of the communication of our wells with the surrounding rock formations. By modeling successive drawdown and recovery curves taken as a

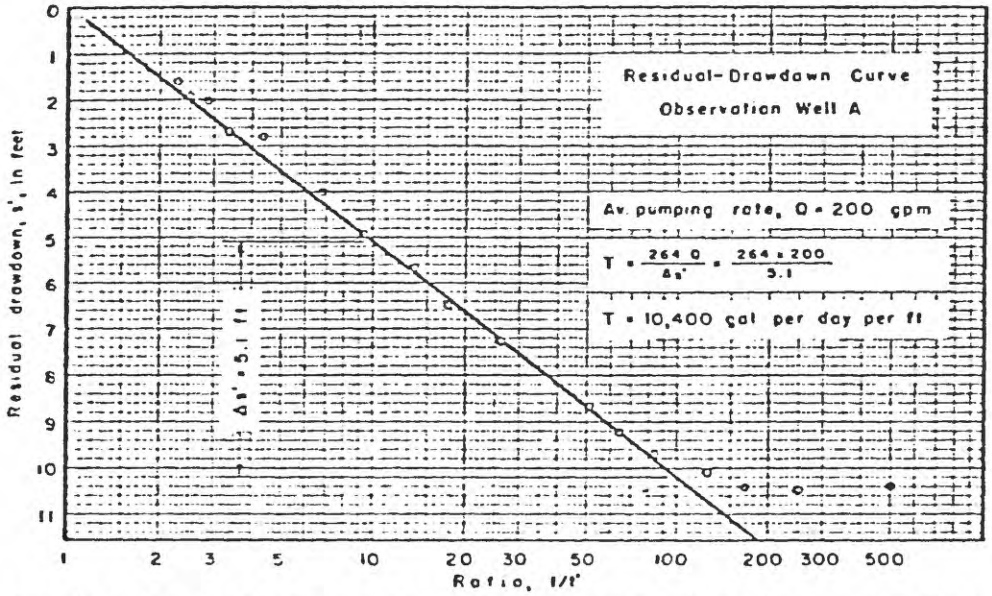

Figure 99. Residual drawdown plotted against the ratio t/t' becomes a straight line on semi-log graph. This plotting permits calculation of transmissibility as shown. Time during recovery period increases toward the left in this diagram.

FIGURE 19

*From Groundwater and Wells, Universal Oil Products Company, St. Paul, Minnesota, 1972.

function of time, we can also obtain the temporal variation of the formation permeabilities. Such information, if not useful as a precursor in its own right, will be helpful in interpreting any observed radon or other geochemistry anomalies observed in the well.

REFERENCES

Davis, S. N. and R. J. M. deWiest (1966), Hydrogeology, J. Wiley and Sons, New York.

Nitsan, U. (1977), Electromagnetic Emission Accompanying Fracture of Quartz-Bearing Rocks, Geophysical Research Letters, vol. 4, no. 8, p. 333-336.

Poreda, R., Y. Chung, J. Lupton, R. Horowitz, and H. Craig, Investigation of radon and helium as possible fluid phase precursors to earthquakes, Trans. Am. Geophys. Union, 59, p. 1196-97, 1978.

Sammis, C. G. (1976), Numerical modeling of hydrothermal reactions in geothermal reservoirs, Proceedings of NSF Geothermal Reservoir Engineering Symposium, Stanford Univ.

Tanner, A. B., Radon migration in the ground: a supplementary review U.S.G.S. Open-file Report 78-1050, 1978.

Teng, T. L. Groundwater radon content as an earthquake precursor, J. Geophys. Res., in press.